22
Soft X-Ray Imaging and Spectromicroscopy

Adam P. Hitchcock

22.1
Introduction

Over the past two decades synchrotron-based soft X-ray imaging techniques have developed into powerful tools for characterization of many different types of samples and phenomena. The suite of such techniques now rivals analytical electron and scanning probe microscopies in terms of breadth of methodologies and applications. It is important to recognize that soft X-ray imaging is a complement rather than a competitor to electron and scanning probe microscopies, typically with unique or superior analytical properties but almost always, lower spatial resolution. As the numbers of soft X-ray microscopy beamlines is steadily growing, access to these facilities is increasingly available. It is now very feasible to plan research strategies that integrate soft X-ray synchrotron imaging with a wide range of laboratory-based nanoscale microscopies, including scanning probe (Chapters 2, 15, 16), transmission electron (Chapters 1, 3-11, 14), and secondary electron (Chapters 17, 25) microscopies, as well as hard X-ray microscopies [1].

This chapter summarizes the most common soft X-ray microscopy techniques and gives insights into the instrumental issues and near future developments, along with selected examples that illustrate the power of each approach. Essentially all techniques described use synchrotron radiation since this is the most powerful and flexible source of soft X-rays currently available. This chapter will not give any general introduction to synchrotron radiation light sources, insertion devices, and beamlines, as these are well described elsewhere [2, 3]. Where specific issues of the X-ray source or beamline are relevant, such as degree of coherence, details are provided. While there are significant efforts to develop competitive laboratory-based soft X-ray microscopes based on higher harmonic lasers [4], laser plasma sources [5], or electron-to-X-ray conversion schemes [6], these are not competitive at present in terms of spatial resolution, intensity, or analytical performance, especially in the arena of nanoscopy.

Handbook of Nanoscopy, First Edition. Edited by Gustaaf Van Tendeloo, Dirk Van Dyck, and Stephen J. Pennycook.

The field of soft X-ray microscopy has been reviewed regularly [7–17] during its development in the past 20–30 years. The more comprehensive reviews include an early overview of all types with emphasis on biological applications [7]; photoelectron imaging [10, 11]; a comprehensive review of methods using energy resolved photoelectrons, along with surface and materials applications [12]; a detailed exposition of the principles and applications of zone plate (ZP)-based microscopes [15]; a review of polymer applications [16]; and a recent focused review of biomaterials applications of X-ray photoemission electron microscopy (X-PEEM) [17]. The textbook, *Soft X-rays and Extreme Ultraviolet Radiation, Principles and Applications*, by David Attwood [3], is essential reading in this field. I will refer to specific reviews or articles for more detailed presentations on specific topics as they are presented. As a complement to this review, I maintain and regularly update a web accessible bibliography (*http://unicorn.mcmaster.ca/xrm-biblio/xrm_bib.html*) of publications in soft X-ray microscopy, which was originally published as a supplement to a review of polymer applications [16].

Soft X-ray imaging methods can be divided into three general types: (i) methods using focused X-rays, with the focusing achieved by mirrors – typically Kirkpatrick-Baez (KB) – or ZPs, including scanning transmission X-ray microscopy (STXM), which is based on the detection of the transmitted X-rays, and scanning photoelectron microscopy (SPEM), which is based on kinetic-energy-resolved detection of the photoelectron; (ii) full-field methods, which include transmission X-ray microscopy (TXM) in which ZPs are used both to control illumination and to project the distribution of the transmitted X-rays to an appropriate area detector and X-PEEM in which the distribution of ejected electrons (both primary and secondary) is magnified using electrostatic and/or magnetic electron magnification lenses and imaged with a suitable X-ray sensitive camera; (iii) coherent diffraction imaging (CDI) methods, in which the far-field coherent scattering signal is measured and inverted into a real space image via a variety of methods. Table 22.1 is a listing of the soft X-ray microscopes available around the world, to the best of my knowledge. Figure 22.1 [18] shows the schematic layout of the common methods of types (i) and (ii). CDI methods are very much at the frontier of soft X-ray imaging and will become increasingly important as fourth-generation light sources come on line and mature. However, this chapter focuses on direct imaging methods and does not cover CDI methods. Readers interested in CDI should consult other articles [19] and reviews [20].

Figure 22.2 [21] shows a conceptual plot of how the various branches of X-ray microscopy and related coherent diffraction (also called "*lensless*") imaging techniques perform with respect to photon energy and spatial resolution. As this handbook focuses on deep submicron resolution (<100 nm) and this chapter deals with soft X-ray techniques, this review deals with techniques that perform within the dotted rectangle in the lower left part of this plot.

Table 22.1 Synchrotron soft X-ray microscopes.

Type	Facility	Name	City	Country	Source	E-range (eV)	Status
TXM	Alba	Mistral	Barcelona	Spain	BM	270–2600	Construction
TXM	ALS	XM1	Berkeley	USA	BM	250–900	Operating
TXM	ALS	XM2 (NCXT)	Berkeley	USA	BM	250–6000	Operating
TXM	Astrid	XRM	Aarhus	Denmark	BM	500	Operating
TXM	BESSY	U41-TXM	Berlin	Germany	Und-L	250–600	Operating
TXM	Diamond	B24 cryo-TXM	Chilton	UK	BM	250–2500	Construction
TXM	NSRL	TXM	Hefei	China	BM	500	Operating
TXM	Ritsumeikan	BL12	Kyoto	Japan	BM	500	Operating
X-PEEM	Alba	Circe	Barcelona	Spain		100–2000	Construction
X-PEEM	ALS	PEEM-2	Berkeley	USA	BM	175–1500	Operating
X-PEEM	ALS	PEEM-3	Berkeley	USA	EPU	150–2000	Operating
X-PEEM	BESSY	UE49 SMART	Berlin	Germany	EPU	100–1800	Operating
X-PEEM	BESSY	UE49 SPEEM	Berlin	Germany	EPU	100–1800	Commissioning
X-PEEM	CLS	CaPeRS	Saskatoon	Canada	EPU	130–2500	Operating
X-PEEM	Diamond	I06	Chilton	UK	EPU	80–2100	Operating
X-PEEM	Elettra	BL 1.2 L	Trieste	Italy	EPU	50–1000	Operating
X-PEEM	MAX-lab	1311	Lund	Sweden	Und-L	100–1400	Operating
X-PEEM	NSRRC	BL05B2	Hinschu	Taiwan	EPU	60–1400	Operating
X-PEEM	Photon factory	BL 18A	Tsukuba	Japan	BM	50–150	Operating
X-PEEM	SLS	SIM	Villigen	Switzerland	EPU	90–1200	Operating
X-PEEM	Soleil	Tempo	Saint-Aubin	France	EPU	50–1500	Operating
X-PEEM	Soleil	Hermes	Saint-Aubin	France	EPU	250–1500	Commissioning
X-PEEM	Spring-8	BL25SU	Hyogo	Japan	EPU	220–2000	Operating
X-PEEM	Spring-8	BL17SU	Hyogo	Japan	EPU	300–1800	Operating
X-PEEM	SRC	Sphinx	Stoughton	USA	Und-L	70–2000	Operating

(continued overleaf)

Table 22.1 *(Continued)*

Type	Facility	Name	City	Country	Source	E-range (eV)	Status
STXM	ALS	5.3.2.2	Berkeley	USA	BM	250–750	Operating
STXM	ALS	5.3.2.1	Berkeley	USA	BM	250–2500	Commissioning
STXM	ALS	11.0.2	Berkeley	USA	EPU	100–2000	Ooperating
STXM	BESSY	old-STXM	Berlin	Germany	BM	250–600	Decommissioned
STXM	BESSY	MAXYMUS	Berlin	Germany	EPU	250–1500	Operating
STXM	CLS	10ID1	Saskatoon	Canada	EPU	130–2500	Operating
STXM	Diamond	I08	Chilton	UK	EPU	250–2500	Construction
(S)TXM	Elettra	Twin-mic	Trieste	Italy	Und-L	250–2000	Operating
STXM	UVSOR	BL4U	Okazaki	Japan	Und-L	50–800	Construction
STXM	NSLS	X1A (2)	Upton	USA	Und-L	250–1000	Decommissioned
STXM	PLS	nanoscopy	Pohang	Korea	EPU	100–2000	Construction
STXM	SLS	PolLux	Villigen	Switzerland	BM	250–750	Operating
STXM	SLS	NanoXAS	Villigen	Switzerland	BM	250–750	Commissioning
STXM	Soleil	Hermes	Saint-Aubin	France	EPU	250–1500	Construction
STXM	SSRF	SXS	Shanghai	China	EPU	200–2000	Operating
STXM	SSRL	13-1	Stanford	USA	EPU	250–1000	Operating
SPEM	ALS	BL 7.0	Berkeley	USA	Und-L	90–1300	Decommissioned
SPEM	ALS	Maestro	Berkeley	USA	EPU	90–1300	Commissioning
SPEM	Elettra	BL 2.2 L	Trieste	Italy	Und-L	200–1400	Operating
SPEM	Elettra	BL 3.2 L	Trieste	Italy	Und-L	27, 95	Construction
SPEM	MAX-lab	BL 31	Lund	Sweden	Und-L	15–150	Operating
SPEM	NSRRC	BL09A1	Hinschu	Taiwan	Und	60–1500	Operating
SPEM	PAL	8A1	Pohang	Korea	Und	20–2000	Operating
SPEM	Soleil	Antares	Saint-Aubin	France	EPU	50–1500	Operating

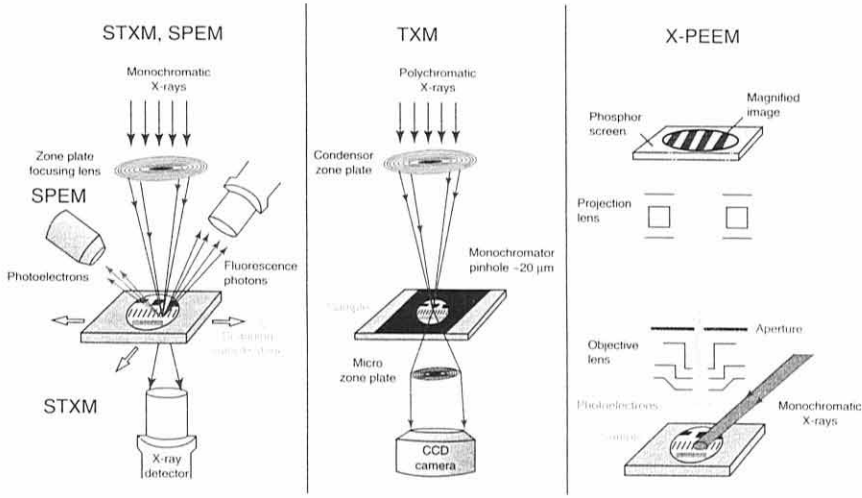

Figure 22.1 Schematic layout of the four common methods of soft X-ray microscopy, which include two focused probe methods, STXM and SPEM, and two full-field imaging methods, TXM and X-PEEM. In each case, the first of the two methods involves transmission of X-rays through the sample and thus is primarily a "bulk" sensitive technique, while the second method involves electron detection and thus is primarily a surface-sensitive technique. (From Ref. [18], used with permission from the author, Joachim Stohr.)

22.2
Experimental Techniques

22.2.1
Full-Field Transmission X-Ray Microscopy (TXM)

This was the original synchrotron-based, soft X-ray imaging technique, developed in the 1960s by Schmal and Rudolf at Göttingen University [22, 23]. The optical layout is analogous to that of a conventional visible light microscope, with a condenser lens used to increase the light density at the sample and an imaging lens to magnify the transmitted light and transfer it to a detector. As indicated in Figure 22.3, a large ZP is used as both a condenser and a crude monochromator to concentrate a narrow band width of the incident X-rays to a few tens of microns, and a micro ZP is used to reimage the X-rays that are transmitted through the sample. Magnification is controlled by the position of the micro ZP and the recording device and by the properties of the imaging micro ZP. There has been a tremendous improvement in the quality of ZPs used for both full-field and scanning microscopes over the past 30 years, with several laboratories producing state-of-the-art ZPs capable of 10 nm imaging [24, 25] and commercial suppliers able to provide ZPs with 25 nm performance. With careful tuning and high-contrast samples, it is possible to

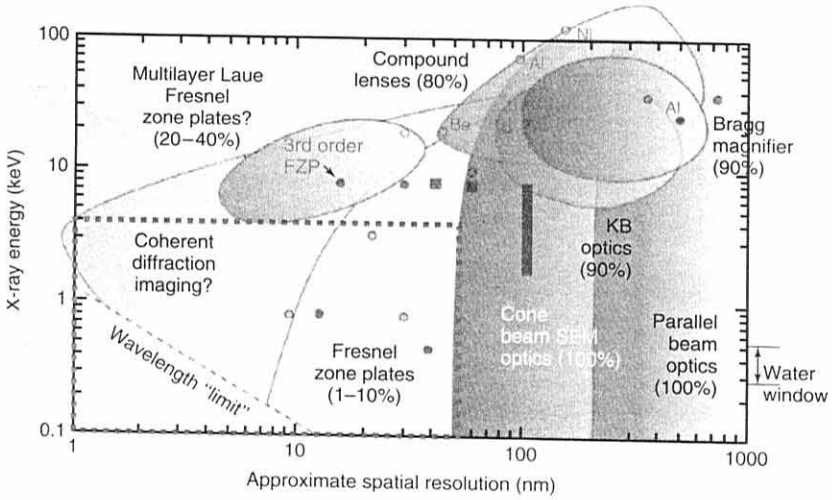

Figure 22.2 Classification of X-ray microscopy techniques based on focusing technologies, achievable spatial resolution, and photon energy range. Points indicate the current capabilities, whereas the shaded zones indicate the range of spatial resolution and photon energies where the technique is applicable as well as the expected potential for spatial resolution. Calculated resolutions are shown with open symbols, measured ones with filled symbols of the appropriate color, circles correspond to synchrotrons, and squares to laboratory sources. See the original article [21] for the sources of the specific performance data. The dotted rectangle indicates the regime relevant to this chapter. (From Ref. [21], used with permission from Materials Today via RightsLink license 2517731089158.)

increase the spatial resolution by using higher diffraction orders of the ZP [26]. Exposure times are typically a fraction of a second up to a few tens of seconds. Although TXMs have the tremendous advantage of parallel detection, there are limitations to the field of view, which is typically between 10 and 30 μm. Mechanical scanning of the sample and tessellation of carefully matched images is used to study wider fields of view.

In general, TXMs produce some of the highest spatial resolution images [25], are excellent tools for magnetic dynamics studies [28–30], and are the preferred method for tomography (see below) but are only rarely used for spectromicroscopy [33–34]. Most TXM instruments are located on bend magnets without any dispersion device other than the condenser ZP. The early applications of full-field microscopes were in water-window biological imaging [35]. More recently, applications have emerged in static magnetism (using off-axis partly circularly polarized X-rays) [27], time-resolved magnetic dynamics [28–30], and a wide range of materials such as cement [31–32]. Until recently, although most bend-magnet sources provide a much wider spectral range of X-rays, almost all TXM research has been carried out in the water window (300–520 eV) in order to study fully hydrated samples. In addition, although TXM condensers act as a crude monochromator, it takes

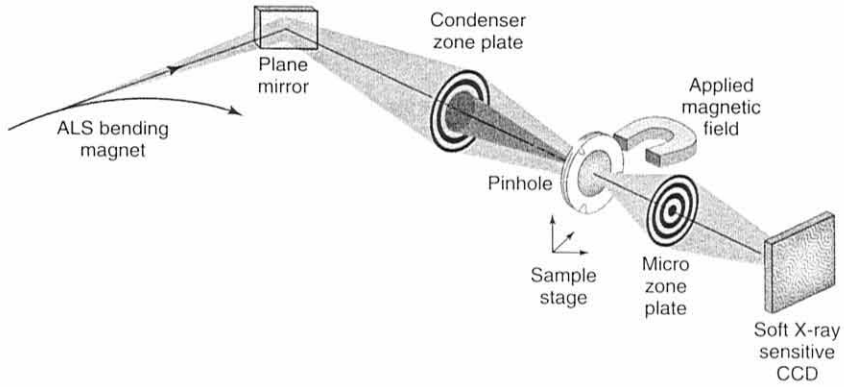

Figure 22.3 Layout of a bend-magnet-based full-field transmission X-ray microscope (TXM, in this case, XM-1 at the Advanced Light Source) [27]. This relatively simple approach provides very high flux and some energy tunability by moving the condenser zone plate. The sample is typically in air (with a short path length to windows enclosing the upstream and down stream optics), which allows relatively straightforward adaptation to modification of the sample environment, as illustrated in this figure, by the applied magnetic field. (From Ref. [27], used with permission from Materials Today via RightsLink license 2534370654740.)

considerable effort to reoptimize the optical setup for different photon energies, and thus most systems have little or no capability to scan the photon energy for spectroscopic applications. A major exception is the undulator-based full-field TXM at the U41 undulator beamline at the Berlin synchrotron, BESSY2 [33]. Soft X-ray undulator radiation has a high degree of coherence, yet the optical principles of TXM require incoherent illumination to avoid artifacts associated with coherent diffraction [36]. The BESSY2 TXM uses a novel rotating capillary optic as the condenser [37] to "bust coherence," thereby allowing use in a TXM of highly monochromated and tunable, but mostly incoherent, light. An alternate approach of rotating a section of condenser ZP has been implemented at the other undulator-based TXM, Twinmic at Elettra [38]. However, to my knowledge, this is not yet set up for spectroscopic full-field studies. Perhaps the most specialized TXM is that of the National Centre for X-ray Tomography (NCXT) at the Advanced Light Source (ALS), which is dedicated to high-throughput water-window tomography. Further discussion of this instrument and its capabilities is given in Section 22.4.3.

22.2.2
Full-Field Photoelectron Microscopy (X-PEEM)

Photoemission electron microscopy (PEEM) is the only soft X-ray imaging technique where there is a larger nonsynchrotron than synchrotron community. Laser or Hg lamp UV illumination is used in laboratory implementations, and topography and work function are the dominant contrast mechanisms. When mounted on a high-performance beam line at the synchrotron, PEEM instruments can exploit

a much wider range of contrast mechanisms, including spectroscopy (elemental and chemical). X-ray linear dichroism (XLD) to study geometric alignment, X-ray magnetic circular dichroism (XMCD) to study ferromagnetism, and X-ray magnetic linear dichroism (XMLD) to study antiferromagnetism. While there are numerous implementations of the commercial instruments at synchrotrons, the two most advanced are custom-built instruments: the spectromicroscope for all relevant techniques (SMART) facility at BESSY2 [39–41] and the PEEM-3 facility at the ALS [42–44]. SMART has implemented aberration compensation electron optics to reduce both spherical and chromatic aberrations [41], with the goal to achieve spatial resolutions below 5 nm with X-ray illumination. PEEM-3 is in the process of implementing a similar system. Figure 22.4 presents a schematic of the electron optical layout of the PEEM-3 instrument at the ALS. Operational since 2008, as of fall 2010, the instrument is in PEEM-2.5 configuration, without the aberration compensation section in the dotted rectangle. Although these two instruments are still under development, the expectation is for very large improvements in efficiency for a spatial resolution in the 50–100 nm range (that of current synchrotron-based X-PEEMs) and to ultimately achieve sub-5 nm spatial resolution with a small percentage of overall transmission (which is a transmission similar to that of current X-PEEM instruments) (Figure 22.4b). These expectations are firmly based on experiences with the performance of analytical aberration-compensated electron microscopes [45, 46]. The SMART system at BESSY2 has achieved better than 4 nm in the low-energy electron microscopy (LEEM) mode of operation [42], which is a truly remarkable performance. However, to my knowledge, the improvements in the spatial resolution and transmission in the X-PEEM mode have not been as good as originally expected. In parallel to the developments at BESSY2 and the ALS, Tromp *et al.* [47] have developed an alternative aberration compensation concept, which has also achieved remarkable performance and is being made available commercially as a combined LEEM/PEEM instrument. I expect significant improvements in X-PEEM performance in the next few years, as these aberration-compensated instruments mature. It should be noted that the ultimate spatial resolution can be obtained only with optimal samples, ones that are totally flat, conducting, and with a uniform potential at the surface.

22.2.3
Scanning Transmission X-Ray Microscopy (STXM)

In a STXM, images are obtained serially by mechanically raster scanning the sample though the focal point of a ZP X-ray lens or (in a few cases) by scanning the ZP and order sorting aperture (OSA) synchronously while the sample is stationary. Figure 22.5a is a schematic of the focusing geometry of a ZP optic. The OSA is required to block the zeroth order (undiffracted) light, which is typically 5–20 times more intense than the first-order focused light. Figure 22.5b,c provides schematics of the polymer STXM [48] at the ALS on beamline 5.3.2.2 [49]. This was the first successful implementation of interferometric control of the (*X*,*Y*)

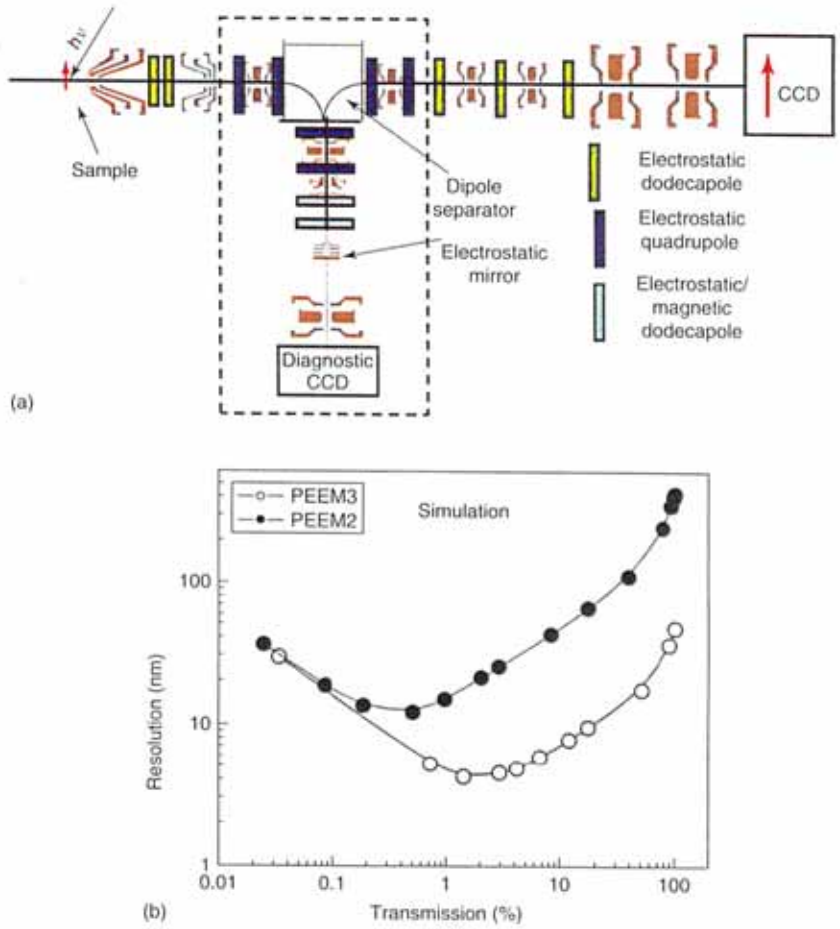

Figure 22.4 (a) Electron optical layout of the PEEM-3 instrument at the ALS [44]. Operational since 2008; as of spring 2011, the instrument is in PEEM-2.5 configuration, without the aberration compensation section in the dotted rectangle. (b) Comparison of predicted transmission of the optics as a function of spatial resolution, with and without the aberration compensation. (Andreas Scholl, private communication, used with permission.)

spatial relationship of the ZP and sample.[1] Similar approaches have now been implemented in other commercial and custom-built soft X-ray STXMs. The quality of the ZP is paramount to the intrinsic resolution capabilities of the STXM (as

1) The first STXM at the NSLS X-ray ring used a nondifferential interferometry system to monitor the (*x*,*y*) position of the sample stage but not the correlation of the sample position with the ZP [50].

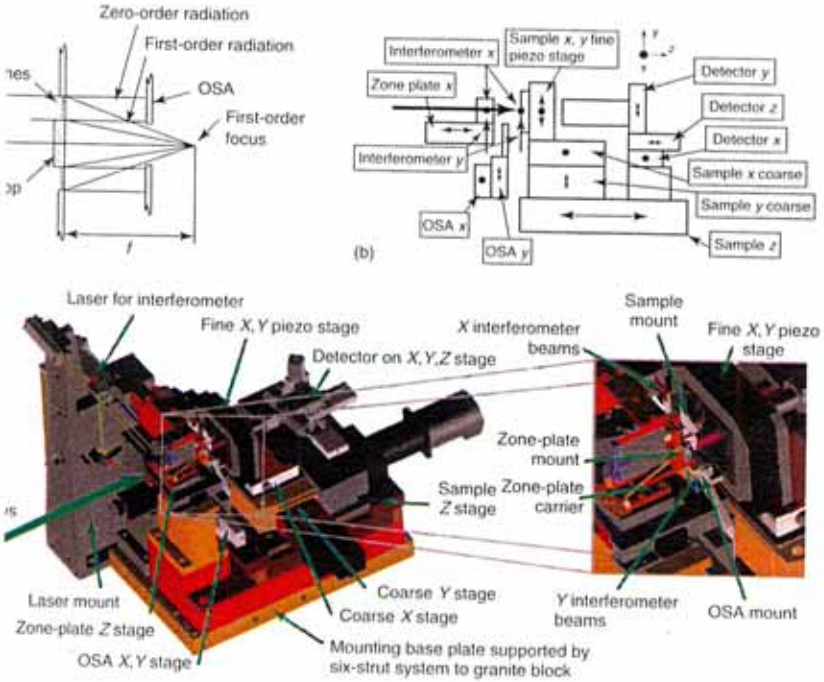

Figure 22.5 (a) Schematic of the focusing in a scanning transmission X-ray microscope (STXM). (b) Schematic of stage motions in the STXMs at ALS, CLS, and SLS. (c) Schematic of the polymer STXM [48] at the Advanced Light Source, beamline 5.3.2.2 [49]. This was the first successful implementation of interferometric control of the (*X*,*Y*) spatial relationship of the zone plate and sample. Similar approaches have been implemented in many other commercial and custom-built soft X-ray STXMs – see Table 22.1. (From Ref. [48], used with permission from IUCr – e-mail from Peter Strickland, 29 Sep, 2010.)

well as SPEM and TXM) and is limited by fabrication technologies that have been slowly but continuously improving over the past decades.

Since ZP focusing is so critical to soft X-ray microscopy, it is worth considering the dependence of the focusing on the ZP properties [3, 15]. A Fresnel ZP is a circular diffraction grating, ideally consisting of concentric metal rings alternating with circular slots mounted on a thin X-ray transparent support. The ZP provides a first-order diffracted beam when the path difference between neighboring open zones is such that the signals from all the open zones reinforce at the focus. To second order (which is a valid approximation at low numerical aperture (NA)), the focusing condition is given by [15]

$$r_n^2 = n\lambda f \tag{22.1}$$

where r_n is the radial position of the nth zone, λ is the X-ray wavelength, and f is the focal length. ZPs are strongly chromatic devices, with the focal length increasing

linearly with photon energy. To get a good focus, the ZP must be illuminated with monochromatic light. The condition to achieve diffraction-limited resolution is given approximately by [51].

$$\frac{\Delta\lambda}{\lambda} \leq \frac{1}{n_z} \tag{22.2}$$

where n_z is the number of zones. Thus, for a ZP with 800 zones (typical of ZPs used in modern STXMs) a resolving power better than 1000 is required. Typically beamlines for STXM are designed to provide a minimum of 3000 resolving power, and the undulator-based STXM beamlines achieve resolving powers of 10 000 or higher, such that there is no problem achieving diffraction-limited performance. However, energy resolution can limit the achievable spatial resolution if the diffraction-limiting apertures (which are usually combined with the exit slit function of the monochromator) are set too wide, in which case resolution degradation will occur. The NA of a ZP is given by [15].

$$NA = \frac{r_n}{f} = \frac{\lambda}{2\Delta r_n} \tag{22.3}$$

where Δr_n is the outer zone width. The diffraction-limited resolution of a ZP according to the Rayleigh criteria [36] is given by

$$\delta_{\text{Rayleigh}} = \frac{0.61\lambda}{NA} = 1.22\Delta r_n \tag{22.4}$$

and the focal length in μm is given by

$$f = \frac{D\Delta r_n}{\lambda} = \frac{D\Delta r_n E}{1239.8} \tag{22.5}$$

where D is the diameter of the ZP in μm, Δr_n is the outer zone width in nm, and E is the photon energy in eV. While the above equations describe the performance of ZPs in first order, ZPs also produce odd higher orders of focusing, with a focal length of f/m, where m is the order of focusing. Thus, when a ZP is operated using its third-order focused spot, the spatial resolution is theoretically three times better than at first order, and with care, this approach can be used to improve spatial resolution [26]. However, the energy resolution needed to achieve diffraction-limited resolution for third-order operation is much higher (×3), and the intensity is much lower, than for first order, such that it is very challenging to find and optimize the third-order focused light from a ZP. Many other issues are involved in fully optimizing the properties and fabrication of high-quality ZPs. These are discussed in great detail in the comprehensive treatment by Howells, Jacobsen, and Warwick [15].

While the ZP optic places fundamental limits on the spatial resolution performance of STXM microscopes (as well as TXM and SPEM), there are many other factors that must be optimized to achieve the focusing potential. STXMs typically involve many high-precision motorized stages for positioning and scanning. These need to be carefully selected to provide the required precision, linearity, and step size resolution. A critical aspect is stabilizing the (*x*,*y*) focal position as photon energy is changed. Since the focal length varies linearly with photon energy (Eq.(4.5)),

a typical near-edge X-ray absorption spectroscopy (NEXAFS) spectral scan of 40 eV width requires a change in the z-position of the ZP or sample of several hundred microns, which must be made with a lateral shift (rollout) much less than the spatial resolution (say, 10 nm). Since the best high-precision mechanical stages (which are needed to give the required range of motion) have rollout figures of 100 nm at best, it is not possible to preserve positioning on the sample by relying only on the properties of the mechanical stage(s) used to set the focal length. Indeed, before the development of interferometric control [48] of STXM mechanisms, drift in the image position was typically a few microns over the course of a 40 eV NEXAFS scan. While this can be largely corrected by software alignment procedures developed for image sequence or stack mode of data acquisition [52], the rollout issue makes point or linescan spectroscopy difficult or impossible, and the software algorithms for alignment have significant limitations, especially when the stack has reversals in image contrast with photon energy. In contrast, when properly tuned, the interferometric controlled STXMs achieve positional stability of better than 50 nm over very large photon energy ranges – typically the full photon range available on the beamline [48]. This active interferometric control approach also provides some compensation for environmental vibrations, typically up to 50 or 100 Hz.

Many different types of detectors have been developed for use with soft X-ray STXMs. These include gas proportional counters [53], phosphor-photomultiplier systems [48], Si photodiodes, avalanche photodiodes, diode arrays [54, 55], and imaging systems [56]. The last two types of detectors are able to provide dark field and phase contrast signals [56], in addition to the bright field signal. High detector efficiency is important to minimize the dose (and thus radiation damage) needed for a given statistical precision. The single photon counting systems typically achieve an efficiency of 30–50%, depending on the photon energy.

An advantage of the photon-in, photon-out character of STXM (and TXM) is that it is possible to operate these microscopes with the X-rays traversing a finite gas path. Thus, most of the TXMs operate with the sample in air, while STXMs typically have the sample and all of the microscope mechanism in a tank that can be evacuated and back filled with He, which is needed to prevent overheating of motors. Aside from the cryo-STXM at the National Synchrotron Light Source (NSLS I) ([57], presently decommissioned), the new MAXYMUS microscope at BESSY2, [58] , and the STXM at beamline 5.3.2.1 at the ALS [59] which are constructed with full ultrahigh vacuum (UHV) technologies, STXMs have been constructed using low-vacuum technologies and lubricated mechanical stages that use volatile organic lubricants. A consequence is that there is a significant problem of carbon contamination of samples when the focused, high-dose-density X-ray beam is left on the same spot on the sample for a time, giving a dose in the giga Gray (GGy) range (which can be a few seconds or even shorter). In order to get around the problem with carbon contamination of samples when using long exposures, as well as to implement some significant advances in the mechanical and controls technologies, a new STXM has recently been developed on a dedicated bend-magnet beamline at the ALS [59]. In addition to use of UHV technologies to

ensure a clean, low-organic environment, it has been designed to scan the ZP as well as the sample, thereby allowing heavy, complex sample mountings, such as that for cryo-spectro-tomography, to be used. In addition, the beam line features an extended photon energy range, from 250 to 3000. The instrument is undergoing commissioning and will be available for general use by the end of 2012.

22.2.4
Scanning Yield Techniques (SPEM, LEXRF-STXM, STM-SXM)

This section describes systems in which a detection channel different from the transmitted X-ray beam is used in a focused probe X-ray microscope. This is typically done to provide sensitivity to a different aspect of the sample, such as its surface, which can be measured with total electron yield (TEY) detection in STXM or by SPEM; electrical properties, measured by electron beam induced current (EBIC) in STXM; optical luminescence properties [60]; or low-energy X-ray fluorescence (LEXRF) measured in STXM [61–65]. An emerging and very promising technique to achieve extremely high (perhaps subnanometer) spatial resolution is to operate a scanning probe microscope (SPM) – typically scanning tunneling microscope (STM) – with zone plate focussed X-ray illumination of the sample–tip junction. Modulation of the X-ray intensity induces a modulation of the STM signal to the extent that X-ray photoionization contributes to the detected signal. Encouraging preliminary results have been obtained at the Photon Factory [66], and the nanoXAS beamline at the Swiss Light Source [68] is dedicated to the development and exploitation of STM–STXM.

When electrons are the detected particle, there is enhanced surface sensitivity. This can be achieved in a STXM simply by measuring the sample current or, with single electron sensitivity, by using a channeltron or channelplate if the vacuum is good enough ($<5 \times 10^{-5}$ torr). While not as sensitive, sample current detection does allow measurements in very poor vacuum (10^{-2} torr), typical of present-generation STXMs. In order to detect electrons with a specific kinetic energy, a time-of-flight (TOF) or dispersive electron spectrometer is required, which necessitates a good high-vacuum or UHV environment in order to minimize inelastic scattering of the photoelectrons before dispersion and detection. Such SPEM [12] are implemented at several synchrotrons (NSRC, Taiwan; PLS, Korea; Elettra, Italy), with the Electra ESCA microscope system being perhaps the best developed and most productive to date. Figure 22.6a shows the basic concept of SPEM [12]. It uses a typical ZP-OSA probe-forming system as also used in STXM. However, in contrast to STXM, where the sample is usually orthogonal to the beam direction, in SPEM the sample is placed at an angle to the incoming X-rays in order to optimize the solid angle seen by the electron energy analyzer. Since the yield of energy-selected photoelectrons is much smaller than the intensity of the transmitted light or the TEY, it is important to have as efficient an electron spectrometer system as possible, which typically means using some type of multichannel detection in the electron analyzer (Figure 22.6b). Because of the low electron yields, the ZP systems used in SPEM are usually selected to have lower spatial resolution and higher

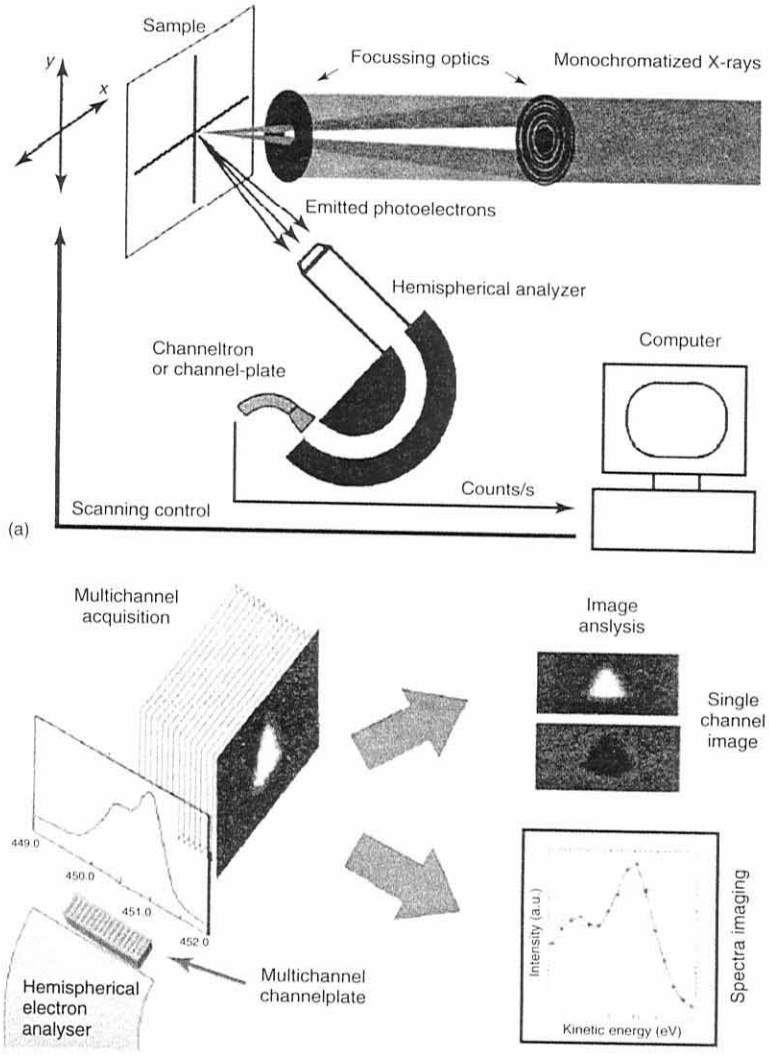

Figure 22.6 (a) Schematic of a scanning photoelectron microscope (SPEM). (b) Schematic of parallel detection in the electron spectrometer to gain efficiency in SPEM. (From Ref. [12], used with permission from Prog. Surf. Sci via Rights Link license 2518440745535.)

efficiency than those used in STXM, typically working at a few 100 nm spatial resolution [12]. Very recently, angular resolved photoemission (ARPES (angle resolved photoelectron spectroscopy)) has been measured in SPEM to study the band structure of materials with submicron spatial resolution (E.E. Rotenberg, private communication). There are beamlines and endstations under development at Elettra, ALS, and Soleil, which will provide sub-100 nm ARPES capability. The new Antares nanoARPES beamline at Soleil has already measured band structures on areas smaller than 100 nm [67].

X-ray fluorescence (XRF) detection in STXM offers a means to greatly improve the detection limits for trace elements in STXM. While XRF has been a major tool in the tender X-ray (2–10 keV) [69] and hard X-ray (10–100 keV) [1] spectral regions, it is only recently that XRF detection has been implemented in soft X-ray STXM. Recently, Kaulich *et al.* [63, 64, 70] pioneered this in the novel Twinmic combined TXM/STXM instrument at Elettra [38]. Figure 22.7 shows a schematic of the

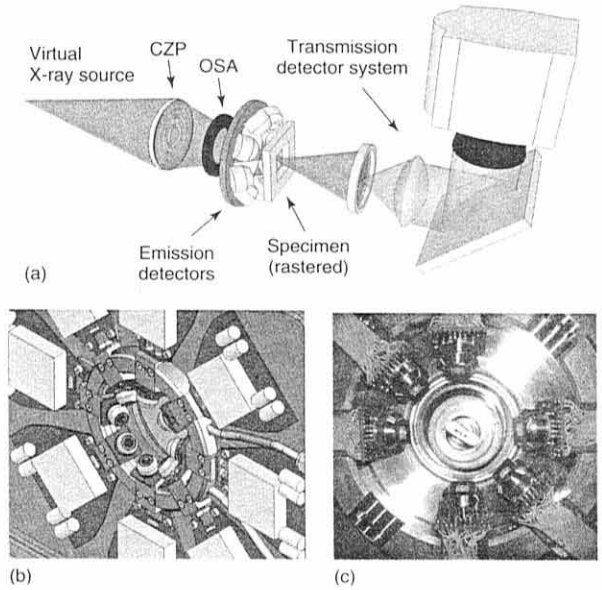

Figure 22.7 (a) Overall schematic of the Twinmic combined TXM/STXM microscope [72] at Elettra. The presample X-ray optics in the layout shown are those for full-field TXM. For STXM, the postspecimen imaging ZP (not shown) is removed and the condenser ZP (CZP) is replaced with a focusing ZP. Special features of Twinmic include a high sensitivity camera as the STXM detector, which allows phase and dark field imaging as well as conventional bright field imaging [56], and an array of silicon drift detectors (SDD) [64] which are used for detecting low levels of elements via low-energy X-ray fluorescence. (b) Schematic and (c) photograph of the six-SDD array currently installed in Twnimic. Each is attached to a water-cooled Cu support and has an advanced pulse processing amplifier directly behind the pnSensor SDD. (Burkhard Kaulich, private communication, used with permission.)

Twinmic set-up, along with a view of the individual silicon drift detectors (SDDs). Currently at Twinmic there is an array of six such detectors which, combined, provide a solid angle of detection of 0.2 sr [64]. Recently, SDDs have been added to the STXMs at the ALS and the Canadian Light Source (CLS). In each case, although the implementation uses only a single SDD, a very effective XRF detection system has been achieved because the detector is only a few millimeters away from the sample as opposed to the 28 mm distance in Twinmic. It is envisaged that there will be significant applications of XRF-STXM in the area of environmental science, where it can be important to detect trace metals for toxicology or other issues. As an example, the ALS system has been used to measure the oxidation state and map the distribution of arsenic in biofilms of Fe metabolizing bacteria (*Acidovorax sp.* strain BoFeN1), which produce copious amounts of various Fe minerals. These species are known to be tolerant to very high levels of toxic As, an important environmental problem in Bangladesh and certain parts of the United States, and *Acidovorax* has been identified in As-contaminated soils. It is not clear whether the accommodation to high As levels is because the As adsorbs to the extracellular Fe minerals or whether the bacteria are actively involved in accommodating to the As by some type of detoxification or biomineralization process. XRF-STXM studies [65, 71] have been able to contribute to this field by mapping the As in these biofilms, which were grown anaerobically for one week with 1 mM As^V in the culture medium. The results from this study (Figure 22.8) very nicely demonstrates that XRF, and especially absorption spectroscopy using XRF-yield, greatly extends the detection limits of STXM. Figure 22.8a compares the X-ray absorption spectrum (XAS) (blue) recorded from transmitted X-rays at the position indicated by the circle on the As map in Figure 22.8c to that measured from the photon energy dependence of the yield of XRF between 1300 and 1400 eV where the Mg Kα and As Lα X-ray emission lines are located (see Figure 22.8b) An advantage of XRF-STXM is that the energy dispersive detector provides maps of other elements, as well as the total absorption, which can provide useful complementary information to the element-specific maps derived from the XRF-yield NEXAFS signal. In this case, the combination of the XRF and XRF-NEXAFS provided maps of the Mg, Fe, and As elemental distributions [65, 71], while the O 1s and absorption signal below the O 1s edge gave maps of the biological material.

A novel development with the potential to dramatically improve the spatial resolution beyond the limitations of current and conceivable future ZP technologies is to combine a focused X-ray probe with a scanning probe implemented as a spatial constraining detector. Eguchi *et al.* [66] were the first to explore this concept but were only partly successful since they had only limited focusing in the Photon Factory end station that was modified to demonstrate XAS detection via an STM tip. Recently, the Swiss Light Source has constructed and is in the process of commissioning the NanoXAS beamline and microscope, a novel combination of a bend-magnet soft X-ray STXM and an SPM [73, 74]. Figure 22.9 shows a schematic of the overall NanoXAS concept as well as a cartoon of photoelectron trajectories under the influence of the applied field from the coaxial SPM tip, which is located at the focus of the ZP. Figure 22.9c shows a STXM image of a

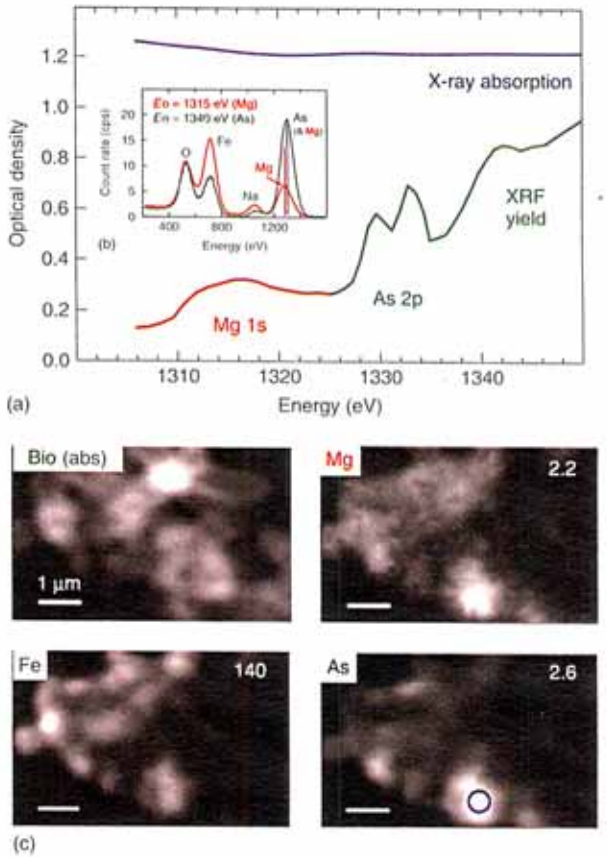

Figure 22.8 Use of X-ray fluorescence to improve sensitivity in studies of minority species such as As in association with *Acidovorax sp.* strain BoFeN1 [65, 71]. (a) X-ray absorption spectrum (blue) recorded with the X-ray beam at the position indicated by the circle on the As map in (c), compared to the NEXAFS spectrum of the same spot measured from the photon energy dependence of the yield of X-ray fluorescence (XRF-yield) between 1300 and 1350 eV. (b) X-ray fluorescence spectrum from the same spot, recorded at two incident photon energies (1315 and 1340 eV). (c) Maps of total absorption and the Mg, Fe, and As elemental distributions derived from XRF. The gray scale indicates counts per pixel for a 180 ms integration time [65, 71].

polystyrene/polymethyl-methacrylate (PS/PMMA) blend recorded at 285 eV, where the PS selectively absorbs, while Figure 22.9d presents topography and phase images recorded in the same region with the *in situ* SPM [68]. The ultimate goal of this instrument is enhancement of spatial resolution by using time modulation of the incident photon intensity and detecting the scanning probe signal in phase at the modulation frequency. At present, the SPM channel provides surface-sensitive

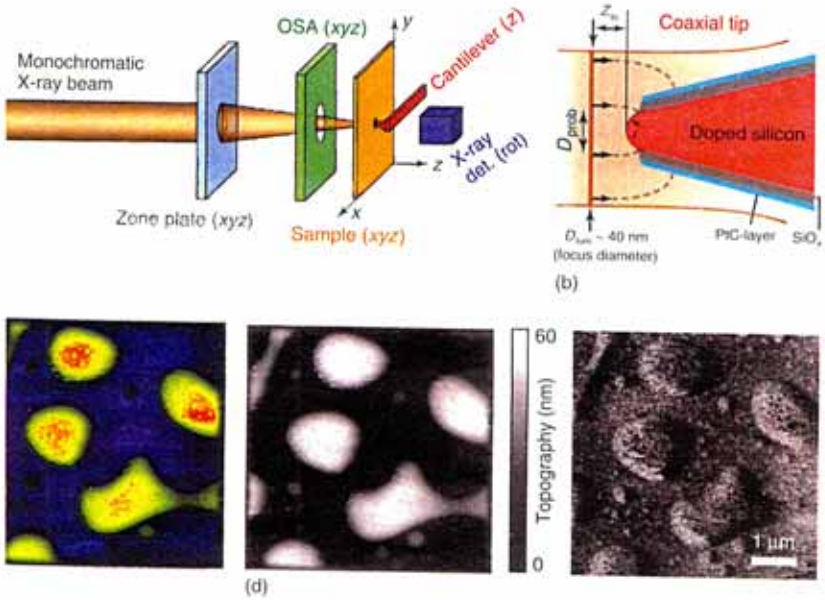

Figure 22.9 Operating principles and images recorded with NanoXAS, a novel soft X-ray STXM combined with an SPM at the Swiss Light Source [73]. (a) Schematic of NanoXAS. (b) Schematic view of the coaxial SPM tip located at the focus of the zone plate indicating the trajectories of the photoelectron under the influence of the applied field. (c) STXM image of a polystyrene-polymethylmethacrylate (PS/PMMA) blend recorded at 285 eV, where the PS selectively absorbs. (d) Topography and phase images recorded in the same region with the *in situ* SPM. The ultimate goal of this instrument is enhancement of spatial resolution by using incident photon intensity modulation and scanning probe pickup at the modulation frequency. At present, the SPM channel provides surface-sensitive imaging and some chemical sensitivity in phase mode, which is complementary to the bulk perspective of STXM. ((a,b) Ref. [73] – used with permission; (c,d) from Christoph Quitmann, private communication, used with permission.)

imaging and some chemical sensitivity in phase mode, which is complementary to the bulk perspective of STXM. Simulations suggest that a resolution well below 5 nm will be achievable [73]. However, at present, there are significant challenges in optimization of the device so as to enhance the modulated signal and suppress background from the parts of the focused X-ray beam that are outside of the pickup region of the SPM tip.

22.2.5
Sample Preparation Issues

For transmission techniques (TXM, STXM), the sample must be partially transparent at the X-ray energies of interest. The optimal thickness is such that the optical

density (OD) at the most intensely absorbing energy is between 1 and 2 OD units. It is best to adapt sample preparation to achieve this if at all possible, rather than struggle with the challenges of absorption saturation in the case of samples that are too thick or that have insufficient contrast in the case of samples that are too thin. Signals below 0.1 OD (down to perhaps 0.01 OD) can be studied if data of sufficient statistical quality is measured. As most samples have an upper dose beyond which the material is too modified for the results to be analytically useful, it is not always possible to use longer times/higher doses or defocusing to build statistics in the case of weakly absorbing samples. The performance for strongly absorbing (nearly opaque) samples in most soft X-ray microscopes is such that there is significant spectral distortion for absorbance levels above 2–3 OD. The upper absorption limit before spectral distortion occurs varies a lot among different instruments since it depends on higher order and stray light content of the incident light as well as detector efficiency and backgrounds. The impact of these factors in turn depends on the details of the NEXAFS spectrum, with spectra having very sharp peaks such as the Ca 2p edge [75] being much more sensitive to absorption saturation artifacts than edges with less sharp features.

Samples for transmission soft X-ray microscopies can be prepared using all of the techniques that are used in transmission electron microscopy (TEM), including ultramicrotomy, cryo-ultramicrotomy, spin-coating, solvent casting, ion beam thinning, and focused ion beam (FIB) milling [76]. Although expensive relative to other methods, FIB is becoming increasingly common, as it allows precise extraction of a sample region of a particular morphology or at a specific spatial location. Modern FIB systems are able to handle materials with dramatically differing densities and toughness, including biological specimens and hard–soft composites that are very difficult to microtome without specimen artifacts. In addition, problems with ion implantation that plagued early FIB samples have been resolved with the addition of low-energy ion polishing techniques as the final stage of the FIB procedure. It is possible to measure single cell prokaryotic biological systems with TXM or STXM without sectioning, which is a considerable advantage over electron microscopic methods, in which biological sample preparation can be chemically complex and may introduce artifacts. Plunge-freeze vitrification is used to preserve microstructure without ice crystal formation during TXM tomography measurements.

For surface-sensitive techniques (SPEM, X-PEEM), UHV compatibility, surface flatness, and conductivity are required. The X-PEEM technique has the most stringent requirements, as there is a very strong electric field at the surface (10–20 kV/mm), which makes X-PEEM extremely sensitive to field emission that is readily induced (and occasionally fatal to the sample) if there are any particles or abrupt changes in topography. Metallographic polishing and metal coating procedures can be used to prepare even very insulating samples such as rocks or teeth for X-PEEM studies [77].

22.2.6
Radiation Damage

Radiation damage is inevitable whenever ionizing radiation is used for microscopy. In order to avoid artifacts in imaging and particularly when making more extensive analytical measurements, it is essential to be aware of the doses at which the sample experiences damage effects that will affect the results of the measurement. If the main goal is to study morphology, it is possible to extend the dose that can be used without artifacts by freezing the sample. This does not change the rate of chemical transformation [78, 79], but it does stop mass loss. Whenever NEXAFS spectra are being used analytically, it is important to determine the dose at which critical spectral features of the most radiation-sensitive component change their intensity because of radiation-induced structural changes. For some polymer materials, this dose can be extremely low – for example, PMMA, and similar esters have a critical dose – the dose to decrease (increase) a spectral feature by $1/e$ $(1 + 1/e)$ – of ~60 MGy [80]. This dose is delivered in less than 100 ms of STXM operation under normal fluxes (10–100 MHz of photons in a 30 nm spot size), which means that damage-free measurements are very challenging. Typically, one must reduce the flux, dose density, or numbers of energy points sampled so that the dose delivered during a measurement of a given area is below 10% of the critical dose. In fact, with chemical amplification, it is possible to image damage in PMMA for exposures of less than 1 ms [81]. Despite these challenges, it is still much easier to perform X-ray absorption spectroscopy of highly radiation-sensitive materials in soft X-ray microscopes than using core level electron energy loss spectroscopy (EELS) in a TEM [82]. Although it depends on the spectral energy range that is required for meaningful analysis, quantitative comparisons [80, 82, 83] suggest an advantage of a factor of 100–1000 for soft X-ray absorption spectromicroscopy over electron energy loss spectromicroscopy at one core level edge, as measured by the G-factor (information/dose).

22.3
Data Analysis Methods

22.3.1
Chemical Mapping – Fitting to Known Reference Spectra

Figure 22.10 shows how quantitative chemical distributions can be derived from soft X-ray microscopy data, in this case a binary thin film blend of PS and PMMA, annealed on a SiO_x substrate, and subsequently transferred to microscopy grids for STXM characterization [84]. Figure 22.10a shows a set of as-recorded transmission images in the C 1s region to illustrate the types of changes in image contrast that occur in multicomponent samples as photon energy changes through the near-edge region. These changes reflect the spatial distribution and the mass–thickness properties of the chemical components. By fitting the spectral signal at each pixel

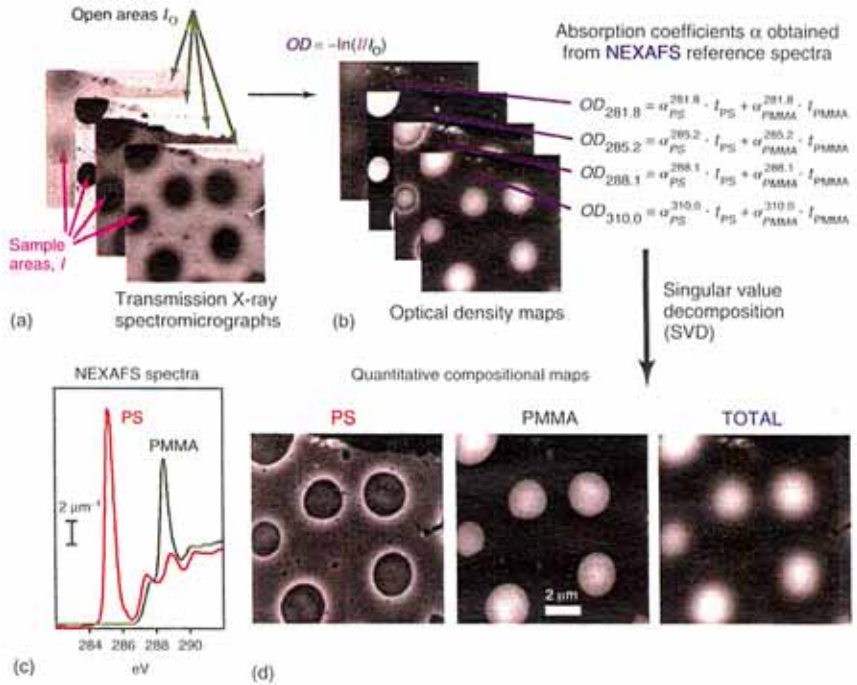

Figure 22.10 Principles of singular value decomposition (SVD) applied to a C 1s STXM image sequence (stack) from a PS-PMMA thin film [16, 84]. The transmission images (a) are converted to optical density (b) and a matrix transform that uses knowledge about the linear absorption coefficients (c) yields quantitative mass–thickness maps (d). (From Ref. [16], used with permission from Polymer via RightsLink license 2518500534762.)

to a linear combination of suitable reference signals (in this case, the C 1s spectra of PS and PMMA), it is possible to invert the set of measured transmission images to quantitative mass–thickness maps of the individual chemical components. If one can make reasonable assumptions about the density, then absolute thicknesses can be derived. The transmission data must first be converted to absorbance or OD using the Lambert-Beer law, $I = I_0\exp(-OD)$. The set of OD images (Figure 22.10b) are then inverted to component maps. There are usually many more spectral points than chemical components (e.g., in this problem, there are only two chemical components but images were recorded at many more than two photon energies). In order to solve the inversion problem, one must have at least the same number of energy points in an image sequence as there are chemical components. More typically, there are many more – a reasonably good sampling of the NEXAFS spectral details can be achieved with 30–100 photon energies if non-uniform energy spacing is used. Quantitative component maps can be derived either by using conventional least squares procedures to fit a linear combination

of suitable reference spectra (Figure 22.10c) to the spectrum at each pixel or by singular value decomposition (SVD) [85], which is an optimized matrix method to invert an overdetermined set of equations, as in this case. There is in general no exact solution to the inversion from measured data to component maps in the case of overdetermined systems. The optimum solution is a "close" result that in some sense satisfies all equations simultaneously. This closeness can be defined in a least squares sense and may be calculated by minimizing the residual error [86]. An illustration of the procedure and outcome is shown in Figure 22.10d. An interpretable model of the PS/PMMA thin film emerges from the SVD analysis. In this case, the analysis shows that the large thick PS droplets are surrounded by a sloping rim of PMMA in such a way that the total film thickness changes smoothly in height. During annealing, PS droplets form, which cannot sink into the PMMA matrix as the film is too thin. This thin film constraint and the balancing of interfacial energies forces the contact line between the PS and PMMA to be relatively high on the PS droplets, leading to a "rim" of PMMA that surrounds the PS droplets. Additional subtleties of the morphology in these thin films could be interpreted using the quantitative information gained from SVD [84].

An extension of the SVD procedure is often useful in cases where there may be some uncertainty about the absolute OD scales of the image sequence or one or more of the reference spectra. This can come about if only the shape and not the absolute intensity of the incident flux (I_0) is used in deriving OD scales. In such cases, scale errors in I_0 are equivalent to constant offsets in OD. Thus "stack fit" is a routine available in analysis of X-ray images and spectra (aXis2000) that automatically adds a constant term to the SVD analysis to compensate [87].

In transmission microscopies (TXM, STXM), the detected signal, after conversion to OD, is quantitatively related to the amount, and thus the intensity scales of the resulting component maps are in units of absolute thickness in nm, if the reference spectra are prepared on a linear absorbance scale (OD per nm of material, under its standard density). In situations such as X-PEEM or SPEM, where the measured intensities are only indirectly related to amounts, or if one does not convert reference spectra to an absolute intensity scale, one can still apply these methods, but the component maps then give information only about spatial distributions and relative amounts. In X-PEEM, if one can measure [80] or estimate the sampling depth for a given system and is comfortable assuming that the work function for

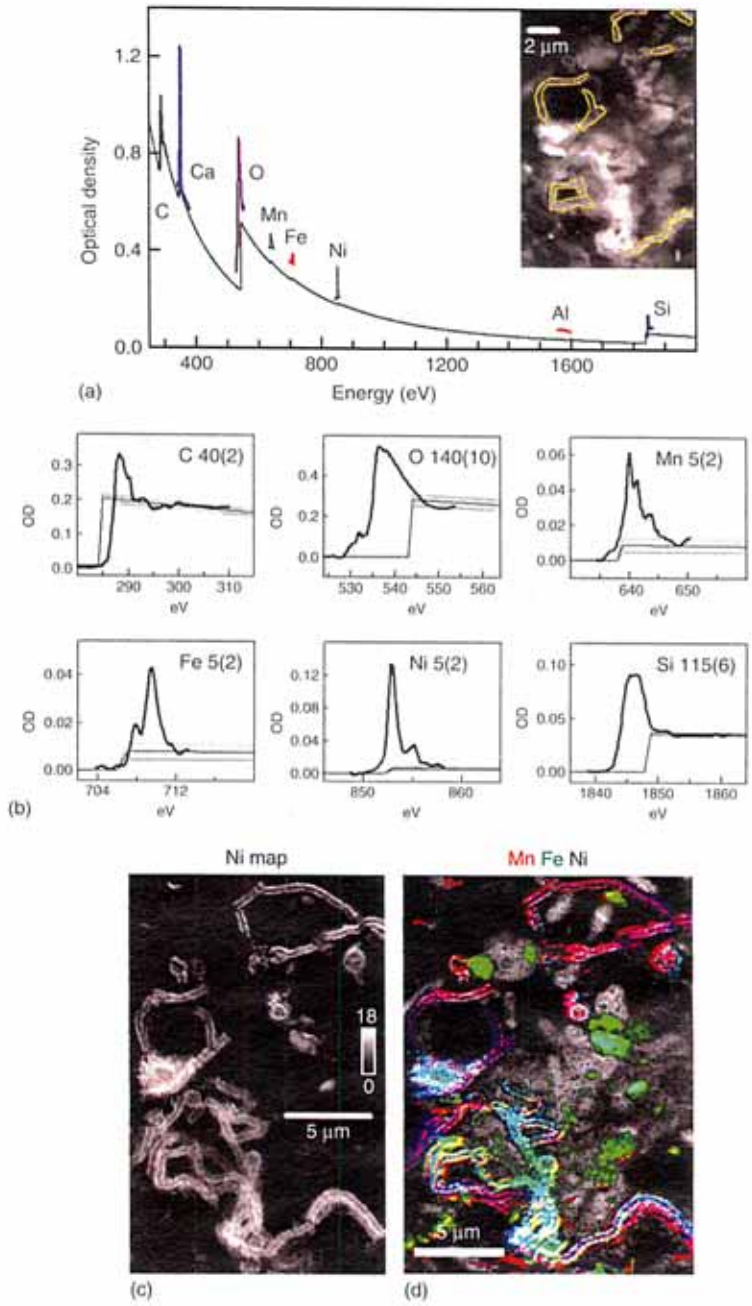

Figure 22.11 STXM analysis of a river biofilm exposed to 10 mg l^{-1} $NiCl_2$ before measurement [88]. (a) Optical density spectrum of the filamentous sheath in a Ni-exposed natural river biofilm (dashed line in the inset image) in the C 1s, O 1s, Mn 2p, Fe 2p, Ni 2p, Al 1s, and Si 1s edges, compared with the sum of the mass absorption coefficients for a best-fit composition. (b) Linear background subtracted spectra of the filamentous sheath at the C, O, Mn, Fe, Ni, and Si edges, along with the elemental edge jump signals (and uncertainties) used to deduce elemental amounts (for further details see [88]). (c) Component map of distribution of Ni (grayscale in nm), derived from two energy imaging at the Ni 2p edge. (d) Color-coded composite of the Mn (red), Fe (green), and Ni (blue) distributions superimposed on the gray scale map of the biology I(288.2 eV) − I(282 eV). (Figures 10 and 11 of Ref. [88], used with permission from Geobiology via RightsLink license 2518500066533.)

different regions of a surface is similar, then quantitative thickness analyses can be performed. An example of this is the quantitative determination of the distribution of proteins adsorbed on a phase-segregated blend surface (see Section 22.4.2).

Figure 22.11 shows a second example of quantitative mapping, in this case a complex environmental sample in which STXM was used to follow mineral and metal ion interactions, possibly mediated by bacterial biomineralization processes, in a natural river biofilm. The biofilm sample, taken from the South Saskatchewan river in Saskatoon, was intentionally spiked with 10 mg l^{-1} $NiCl_2$ during a 24 h period before the analysis to explore how different species accommodate toxic Ni^{2+} ions [88]. NEXAFS image sequences were measured for nine different elements (C, Ca, O, Mn, Fe, Ni, Na, Al, and Si). The inset image in Figure 22.11a shows a STXM image of a region of the biofilm where there is a variety of bacteria, both individual cells and groups of cells enclosed in a filamentous sheath. The metal ions were found preferentially in association with the filamentous structures, although there are also Fe-rich mineral grains in the field of view. The absorption spectrum at eight edges of the filamentous structure, taken from the identical area indicated in yellow outline in the inset in Figure 22.11a, is shown in Figure 22.11a, along with the elemental response expected for the average composition determined by SVD fits of the spectrum at each edge to appropriate reference spectra. Independent of the assumptions about chemical speciation (which can be challenging in a complex system like this), one can determine the elemental composition from the edge jump, as indicated in Figure 22.11b, where the edge jump for the determined composition, along with an error range, is plotted along with the average edge spectrum of the filaments. Figure 22.11c shows the quantitative Ni map, where the maximum thickness is only 18 nm, and the average thickness, mapped as NiO, (in an area determined to be Ni-rich), is less than 3 nm. Figure 22.11d is a color-coded composite of the Mn, Ni, and Fe signals. The Ni is found in association with Mn and Fe and is believed to accumulate through abiotic processes on Fe–Mn minerals created by biomineralization [88].

It is noteworthy that approaches similar to those outlined above – forward fitting by use of SVD or stack fit to derive relative or absolute quantitative maps from image sequences – can be used to analyze other types of image sequence signals, where a parameter other than incident photon energy is scanned. Examples include XRF maps (see Section 22.2.4) and linear dichroism maps (see Section 22.4.1) – the dependence of image contrast on the orientation of the E-vector of the soft X-rays relative to a sample at a given photon energy. Such sequences can be fit to the known functional response of linear dichroism, $I(\theta) = C + A\cos^2(\theta - \theta_{ref})$, where $I(\theta)$ is the intensity at a given E-vector angle, C is an angle-independent term, A is the amplitude of the angle-dependent signal, which has its maximum signal when $\theta = \theta_{ref}$, where θ_{ref} is the angle where the transition intensity is maximum (for 1s excitation, this corresponds to having the E-vector aligned with the transition moment vector, which, in simple systems, can be the direction of orbitals of the upper level to which the 1s electron is excited). This methodology is included in aXis2000 [87] and has been used to map distributions of β-sheet crystallites in dry and wet dragline spider silk [89, 90] and of sp^2 defects in carbon nanotubes [91–92, 93], in addition to the example given in Section 22.4.1.

22.3.2 Chemical Mapping – Unsupervised Statistical Analysis Methods

A concern with the types of forward fitting analyses described in the previous section is that they require prior knowledge of the chemical components present in the system under study. In many cases, this information is not available, or only some of the chemical species are known. Given the highly overdetermined nature of soft X-ray microscopic image sequences, it is of interest to consider multivariate statistical analysis (MSA) methods [94] that look for patterns in complex data of this type. MSA-based methods can be used for many aspects of the analysis: to identify the number of statistically valid chemical species that might be present; to derive meaningful reference spectra; and to convert the image sequence to quantitative chemical maps. The merit of this approach is that it provides a means to perform a "standard-less" analysis that effectively uses the highly redundant nature of the spectral domain information. Typically a STXM image sequence consists of $10^4 - 10^5$ spectra, for systems in which it is statistically meaningful to identify only five to seven components. Chris Jacobsen has provided the X-ray microscopy community with a useful tool for this type of analysis [95]. The procedure (PCA_GUI [96], which is embedded in aXis2000 [87]) first performs a principle component (PC) analysis, which identifies power-weighted eigenspectra and associated eigenimages. The user then selects an appropriate number of PCs to further process the data with a cluster analysis, which is a procedure to find a means of combining the PCs in such a way that they group together into clusters in "PC-space." These cluster spectra are typically much closer to true NEXAFS spectra of chemical components, although it is not always true that the cluster approach gives valid spectra and thus chemical identification. An added advantage of this approach is that a very significant noise reduction is achieved by restricting the analysis to include only the most significant PCs (typically 5–10, in a data set where the number of PCs (eigenspectra) is equal the number of pixels in each image). After rotating the PCs by identifying clustering in the PC-space, these reference spectra can be used in a final target analysis step to derive the chemical maps, which can be made quantitative or semiquantitative if the user supplies appropriate information about chemical composition and density. A very useful feature of the target analysis phase is that the spectra of chemical species known to be present can be introduced at this point, which often greatly improves the overall analysis.

Figure 22.12 presents results from analysis of a C 1s image sequence of a microtomed section of a core-shell microsphere composed of a divinyl benzene (DVB) core covered with a shell composed of a 50 : 50 DVB – ethylene glycol dimethylacrylate (EGDMA) mixture [97]. In this case, the PC analysis clearly indicates that only three statistically significant components were present. The reference spectra derived from the cluster analysis are displayed in Figure 22.12b, while three cuts through the PC-space (C1 vs C2, C1 vs C3, and C2 vs C3) (Figure 22.12b) show that

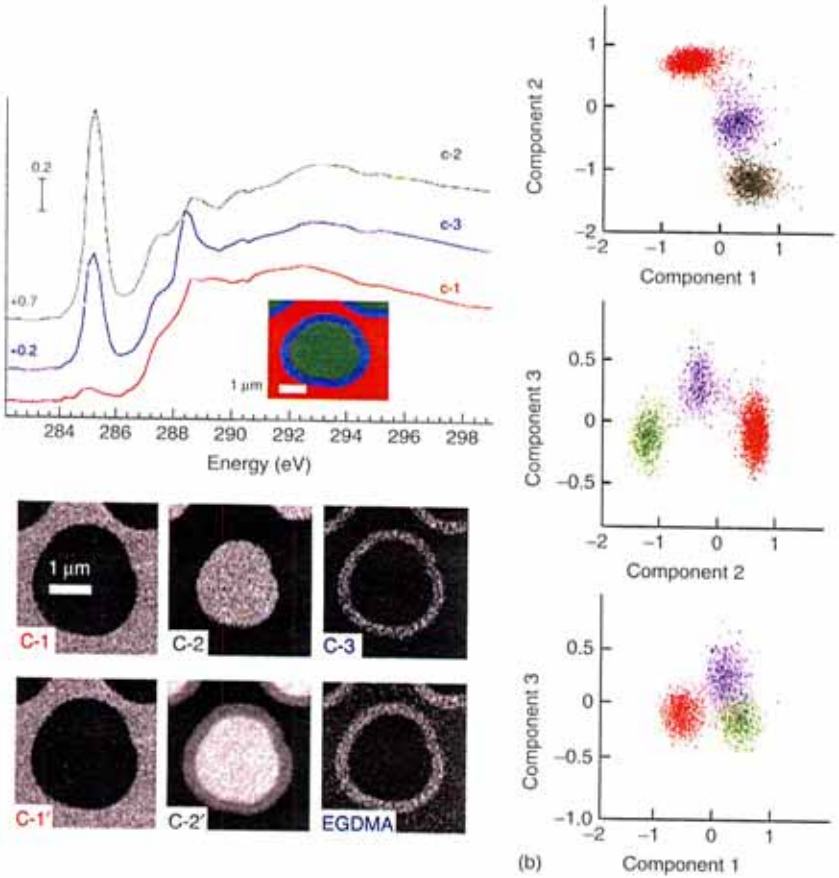

Figure 22.12 Results of a multivariate statistical analysis using a combination of principle component and target analysis applied to C 1s STXM results for a microtomed section of a core-shell microsphere [97]. (a) Rotated principle component spectra derived by PCA followed by a Euclidean cluster analysis [95]. Cluster 1 matches epoxy, and cluster 2 matches divinyl benzene (DVB). (b) Cluster plots of PC1 vs PC2; PC2 vs PC3, and PC1 vs PC3. (c) Component maps derived using the C-1, C-2, and C-3 target spectra. (d) Component maps derived by replacing C-3 target with the measured spectrum of ethylene glycol dimethylacrylate (EGDMA). Note the shell is known from the synthesis to be ~50 : 50 DVB:EGDMA. (From Ref. [16] used with permission from Polymer via RightsLink license 2518500534762.)

the cluster analysis (Euclidian metric) produced a very clean grouping of the data into three spectra and that the resulting spectra are very plausible NEXAFS spectra. The spectrum for component 1 is identical to that of epoxy resin, and that for component 2 is identical to that of DVB. Unfortunately, the spectrum for component 3 is identical to that of the shell, which is known from the material synthesis to be a composite of DVB and EGDMA. Thus, when these cluster spectra are used to fit the data, the result is simply a separation into the 3 spatial components (Figure 22.12c), without a clear indication that the shell is a mixture of two chemical species. When the spectrum of EGDMA is introduced in the target analysis step instead of component 3, the resulting maps (Figure 22.12d) are correct and provide the same answer as that from SVD. Both forward fitting analysis and MSA are valuable tools for the interpretation of soft X-ray spectromicroscopy data sets. It is usually wise to examine critical data sets with both approaches. A limitation of both approaches is that they always give an answer. It is essential that the analyst probes these answers to verify that they indeed represent the actual chemistry of the sample. Threshold masking techniques are provided in aXis2000, which allow extraction of the spectra associated with specific pixel subsets, defined on the basis of intensities in component maps derived by either forward fitting analysis or MSA. It is generally a good idea to extract such spatially selected spectra and investigate the quality of the analysis in spectral space. Counterparts to both SVD and stack fit stack analysis routines for fitting individual spectra are provided in aXis2000 for this purpose.

22.4
Selected Applications

22.4.1
Polymer Microstructure

Soft X-ray spectromicroscopy is optimally suited to study multicomponent polymer systems since (i) NEXAFS at the C 1s and other edges is well suited to differentiate even very chemically similar polymers [13, 98], (ii) many phase-segregated blends of technical and commercial importance have domain sizes easily resolved by current instruments, and (iii) electron beam analysis methods such as EELS in TEM have lower energy resolution (and thus are less able to differentiate species) and are significantly limited by the higher rate of radiation damage per unit analytical information [83]. Polymer microstructure analysis by soft X-ray microscopy is an application where there is significant industrial involvement, such as work on basic understanding of nanostructure of polyurethane foams [99, 100], superabsorbent gels [101], polymer reinforcements [102], and modification of polymer properties [103–105]. While the published work in this area tends to be fundamental, there are many cases where unpublished soft X-ray microscopic studies have played an important role in troubleshooting processing problems or assisting development of new or improved polymer processing.

A topical example of polymer analysis by STXM is in the area of organic solar cells. In contrast to semiconductor-based solar cells, the goal for organic solar cells is modest photoyields but ultralow cost fabrication [106]. Working devices must achieve a bicontinuous phase separation of donor and acceptor polymers with a mean size of the order of the exciton length (<10 nm) such that there is efficient separation and independent transport of the electron and hole generated by the

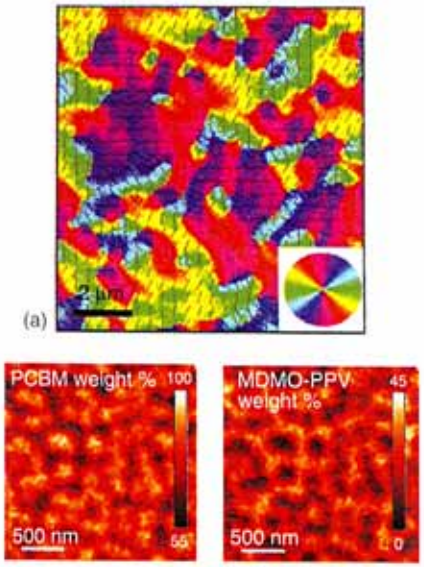

Figure 22.13 Example of linear dichroism mapping using STXM [109]. (a) In-plane molecular orientation map of an annealed thin film of poly(9,9 δ-dioctylfluorene-co-benzothiadiazole) (F8BT) derived from the linear dichroism at the C1s $\rightarrow \pi^*$ transition (285 eV) measured by sample rotation with a fixed horizontal E-vector. The π^* resonance is perpendicular to the polymer backbone, whose orientation in each domain is indicated via the black lines, the length of which indicate the estimated, fully extended length of the polymer backbone [109]. (b) Mapping the weight percentage composition of poly[2-methoxy-5-(3′,7′-dimethyloctyloxy)-1,4-phenylene vinylene] (MDMO-PPV) and (6,6)-phenyl-C_{61}-butyric acid (PCBM) in a 1 : 4 (w/w) blend (MDMO-PPV:PCBM) thin film, derived from images recorded at four energies (280, 284.4, 287.4, and 320 eV) [108]. (From B. Watts, private communication, permission granted.)

incident light. STXM is being applied to assist materials optimization in this area [107, 108]. Figure 22.13 presents two aspects of this work. The first demonstrates the ability of the linear dichroic signal in STXM microscopy to determine molecular orientation and domain structure in these types of materials. The second demonstrates imaging phase separation in a viable organic solar cell material. By recording images at a resonant photon energy with multiple sample orientations, the linear dichroism of an annealed thin film of poly(9,9-dioctylfluorene-co-benzothiadiazole) (F8BT) can be fit to a model to reveal the dominant molecular orientation within each pixel [109]. Figure 22.13a shows the in-plane orientation derived from the intensity of the C1s->π^*(285 eV) – the color wheel in the inset indicates the correlation of color and orientation. The π^* resonance is perpendicular to the polymer backbone and thus the orientation of the polymer backbone can be determined. It is indicated via overplotted black lines, the lengths of which indicate

the estimated fully extended length of the polymer backbone. Figure 22.13b shows maps of poly[2-methoxy-5-(3′,7′-dimethyloctyloxy)-1,4-phenylene vinylene] (MDMO-PPV) and (6,6)-phenyl-C_{61}-butyric acid (PCBM) in a 1 : 4 (w/w) blend (MDMO-PPV:PCBM) thin film. These maps were derived from images recorded at only four energies (280, 284.4, 287.4, and 320 eV), selected for their ability to differentiate these two species [108]. Such maps provide very useful feedback on the extent to which the desired interpenetrating continuous phase is actually achieved. The spatial resolution of the present STXM microscopes (20–30 nm) is still a little too coarse for this application, which really needs imaging of acceptor and donor domains, which are required to be within ~10 nm of each other. Improvements to ZPs [25] and development of other soft X-ray imaging methods such as ptychography [110] as well as complementary chemically sensitive resonant scattering techniques [111, 112] are important to further progress in this area.

22.4.2 Surfaces and Interfaces

Magnetic materials are a critically important aspect of modern information storage and processing technologies. Soft X-ray microscopic and spectroscopic methods to study magnetism and magnetic dynamics are described in detail in the monograph by Stöhr and Siegmann [18]. The current generation of high-capacity hard disk storage systems relies heavily on research results obtained with synchrotron soft X-ray microscopies, spectroscopies, and dynamics measurements. Read–write heads exploiting giant magnetoresistance, out-of-plane recording media, and nanopatterned storage media all have benefited from soft X-ray microscopic and spectromicroscopic studies. As the performance continues to improve exponentially, increasingly small volumes of magnetic materials, with carefully controlled nanoscale materials chemistry are key. Nanoscale methods for their characterization are essential. Here, I give two examples, one based on polarization-dependent X-PEEM studies and the other using X-PEEM to investigate protein biomaterial interactions.

Interactions of ferromagnetic and antiferromagnetic domains are critical in the "pinning" of specific regions in complex magnetic sensors such as giant magnetoresistance heads, but the magnetic exchange interaction is quite complex and can be mediated or complicated by crystallographic effects. Figure 22.14 shows magnetically and structurally sensitive PEEM images recorded at specific Ni 2p and O 1s resonant peaks of the near-surface region of a polycrystalline sample of a NiO(001) surface [113]. Comparison of the contrast in identical regions reveals a complex interplay of crystal structure – orientation of the grains as deduced from the O 1s XLD – and antiferromagnetic magnetic order – as deduced from the Ni 2p linear X-ray linear magnetic dichroic (XLMD) signal. When a thin ferromagnetic Co layer is deposited on this surface, there is a perpendicular coupling between the Ni and Co moments. The chemical interactions at the Co-NiO interface drives a crystallographic transformation leading to reorientation of the Ni moments from the <112> to the <110> direction [113]. Detailed nanoscale dichroic studies show that the reorientation is driven by changes in magnetocrystalline anisotropy rather

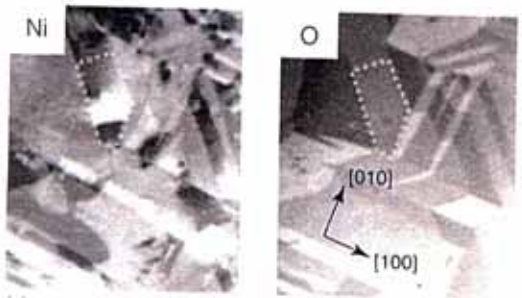

Figure 22.14 X-PEEM images (ALS PEEM-3) of the near-surface region of a Ni(001) single crystal recorded at (a) the Ni $2p_{3/2}$ resonant peak showing X-ray linear magnetic dichroic contrast (XLMD) and (b) at the O 1s resonant peak showing X-ray linear dichroic contrast (XLD). Field of view is 8 µm. From the O 1s signal, the region outlined the dotted lines appears crystallographically to be a single domain, whereas the Ni 2p XMLD shows there is a complex magnetic domain structure within this and other individual crystal domains [113]. (From Hendrik Ohldag, private communication, permission granted.)

than exchange coupling. An additional example of magnetically sensitive soft X-ray microscopy in given in Section 4.4.4, where time-resolved XMCD-STXM is used to exemplify *in situ* conditioning of samples.

The second example of surface and interface applications of soft X-ray microscopy is in the area of soft materials, which are traditionally very difficult to study with electron-beam-based techniques. Figure 22.15 shows results from a combined C 1s and N 1s X-PEEM study of the adsorption of human serum albumin (HSA) on to a phase-segregated bend of PS and polylactic acid (PLA) [114]. This is part of a recently reviewed [17] set of X-PEEM studies of protein interactions with phase-segregated polymer blend surfaces, which are candidate biomaterials for use in medical application. The ~50 nm thick, 40 : 60 PS:PLA blend film is spun coated on a Si wafer (0.7 wt% in toluene), annealed 6 h at 45 °C and exposed to a 0.005 mg ml^{-1} aqueous solution of HSA for 20 min. The colorized individual component maps are displayed across the top (Figure 22.15a–c), while Figure 22.15d is a rescaled color-coded composite of the derived component maps for HSA (blue) – from N 1s edge, PS (red), and PLA (green). This example nicely illustrates the advantage of using spectroscopic information from multiple core levels to improve sensitivity to specific components.

22.4.3
3D Imaging (Tomography) and 3D Chemical Mapping (Spectrotomography)

For the thin samples typical of soft X-ray transmission microscopy (TXM or STXM), 2D projection imaging is often sufficient. However, for thicker, low-density samples, such as biological or environmental samples, one needs information about the *z*-position of the absorbance in order to properly interpret the image and

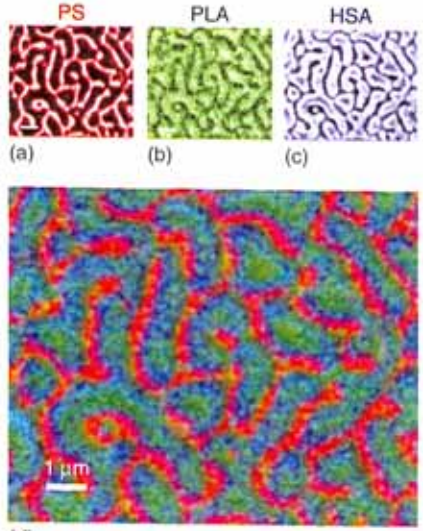

Figure 22.15 Analysis of protein (human serum albumin HSA) interactions with a polystyrene-polylactic acid (PS-PLA) polymer blend surface by C 1s and N 1s image sequences recorded in X-PEEM (ALS PEEM-2) [114]. The main image is a rescaled color-coded composite of the derived component maps for HSA (blue) – from N 1s edge, PS (red), and PLA (green). The ~50 nm thick, 40 : 60 PS:PLA blend film is spun coated on a Si wafer (0.7 wt% in toluene), annealed 6 h at 45 °C and exposed to a 0.005 mg ml^{-1} aqueous solution of HSA for 20 min. (From Ref. [114], permission granted from ACS Biomacromolecules via RightsLink license 2518430179156.)

spectromicroscopic information. A simple way to achieve this is to record stereo pairs with the sample tilted between the two images by 10–30° [115]. However, for more complex cases, as in congested cells with many morphological elements distributed in 3D over a thickness of 1–3 µm, the better approach is to do a complete 3D visualization by serial section imaging [116] or angle scan tomography [117]. Full-field TXM is the most developed type of soft X-ray tomography. Samples can be loaded fully wet into pulled glass capillaries or mounted on whole or sections of TEM grids. The capillary approach is preferred not only because it allows full 180° rotation and thus avoids the "missing wedge" artifacts that exist with reduced angular range tomograms but also because it is a good way to retain fully wet samples in the case of room temperature studies and it is compatible with plunge-freeze vitrification techniques for cryotomography. The latter has become the accepted approach for both electron and X-ray tomography of biological samples since the plunge freezing prevents generation of large ice crystals that destroy the microstructure and the frozen samples do not suffer mass loss while recording the tomograms (although it is important to note that chemical damage from absorption of X-rays occurs at the same rate as at room temperature [79]).

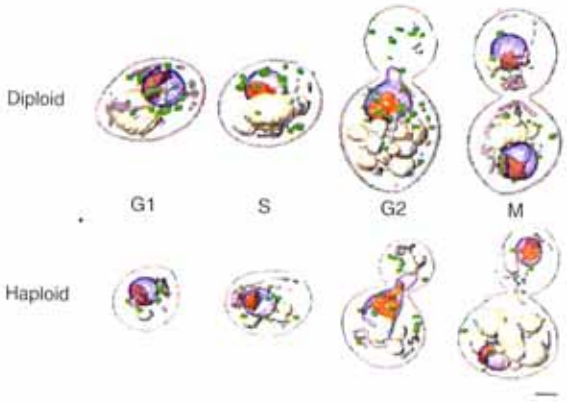

Figure 22.16 Three-dimensional images of *S. cerevisiae* yeast cells at different phases of the cell cycle [118], measured with the National Center for X-ray Tomography (NCXT) full-field cryo X-ray tomography instrument at the ALS. The top row shows diploid cells, whereas the bottom row shows haploid cells. Organelles are identified based on mass absorption at ~520 eV, and are color coded: nucleus, blue; nucleolus, orange; vacuoles, ivory; mitochondria, gray; lipid bodies, green. Scale bar is 1 μm. (From Ref. [118], used with permission from Yeast via RightsLink license XXXXX.)

At present, the most advanced facility for high-throughput soft X-ray tomography of biological samples is the NCXT at the ALS. Figure 22.16 shows results from a recent NCXT study [118] of the internal structure of *Saccharomyces cerevisiae* yeast cells at different phases of the cell cycle, derived from tomograms on eight different cells, measured at a single photon energy (~520 eV, in the water window). The top row shows diploid cells, and the bottom row shows haploid cells. The color coding of the internal structure is based on segmentation – differentiation on the basis of mass absorption at ~520 eV. The organelles are color coded: nucleus, blue; nucleolus, orange; vacuoles, ivory; mitochondria, gray; lipid bodies, green. As larger amounts of data are accumulated, it is very likely that this segmentation approach will produce very valuable insights into the internal structure of micron-scale biological organisms. Excellent work on studies of the 3D structure of biological specimens is also being carried out at the BESSY2 TXM facility, for example, the first study of mammalian tissue [119] and a recent study of the structure of *Vaccinia* virus [120].

If the full-field tomograms could be measured at a number of different photon energies, a more explicit connection between X-ray microscopic signal and chemical identification could be achieved. To date, the only full-field TXM system able to perform high-quality spectroscopy and spectrotomography is that at BESSY2 [34, 37]. Another approach to obtain 3D imaging is to carry out tomography in STXM. Although much slower than full-field TXM tomography, the superior spectroscopic capabilities of STXM provide an added dimension worth exploiting. Pioneering STXM tomographic experiments were done at NSLS [121], and the Stony Brook group developed and operated a UHV cryo-STXM for tomography at X-1A beamline at NSLS [122]. However, those earlier STXM tomographic studies used only a single

photon energy, so they did not take advantage of the spectroscopic power of STXM. Recently, room temperature spectrotomography based on imaging over multiple photon energies and a range of sample orientations has been implemented in STXM. Measurements have been reported on wet samples in pulled glass capillaries [123] as well as dry samples on grid sections [124–126]. Although the glass capillary approach has the advantage of being able to measure the full 180° angular range, and thus does not suffer from "missing wedge" artifacts, to date it has not been able to prepare walls sufficiently thin to work at X-ray energies below 340 eV. In contrast, while the grid method typically can only be applied over ±70°, it has been possible to measure tomograms at energies as low as the S 2p region (150–180 eV) [126].

To illustrate the ability of STXM spectromicroscopy to provide quantitative 3D chemical mapping, Figure 22.17 shows results from a STXM spectrotomographic study of polyacrylate-filled PS latex microspheres in water in a pulled glass capillary [123]. Figure 22.17a is a single projection image at 530.0 eV, below the onset of the O 1s absorption. While this projection image shows the shell structure of the microspheres, the boundaries of the microspheres and the capillary are blurry because of curvature. After reconstruction of the tomogram from a set of 60 images (0–180°) at two photon energies (530.0, 532.0 eV), a much clearer view of the structure is obtained (Figure 22.17b). The difference in the OD at these two energies was used to quantify the amount of polyacrylate in each voxel, while the signal at 530 eV can be segmented to separately identify the glass wall, the water, and the PS shell. Figure 22.17c is a colorized rendering of the tomographic reconstruction in which the PS (red) and water (blue) are differentiated by OD at 530 eV; the glass wall has been removed, and the acrylate (green) is identified spectroscopically by the difference in OD at 532 and 530 eV. Figure 22.17d shows a quantitative projection of the tomogram of only the acrylate component in which the blue color scale corresponds to 2–8 nm of acrylate through the projected path while the green color scale corresponds to 8–15 nm in the projection. This type of information, in particular the ability to generate statistics on fill levels, rupture, and internal distributions over a number of different latex microspheres, is valuable feed back to the industrial partner in this study.

22.4.4 *In situ* Techniques

In recent years, a major thrust in the development of soft X-ray microscopies has been *in situ* studies, in which the properties of a sample are manipulated in some way while it is still in the microscope. When seeking information about structure–function relationships, *in situ* studies are highly desirable, as they can provide a very direct link between the nanostructure and how it can affect a particular process or how the nanostructure can be modified by a particular external stimulus. While there are examples in the literature of *in situ* experiments with all four types of soft X-ray microscopy this review has discussed, the TXM and STXM techniques are those with the most extensively developed *in situ* technologies because of the

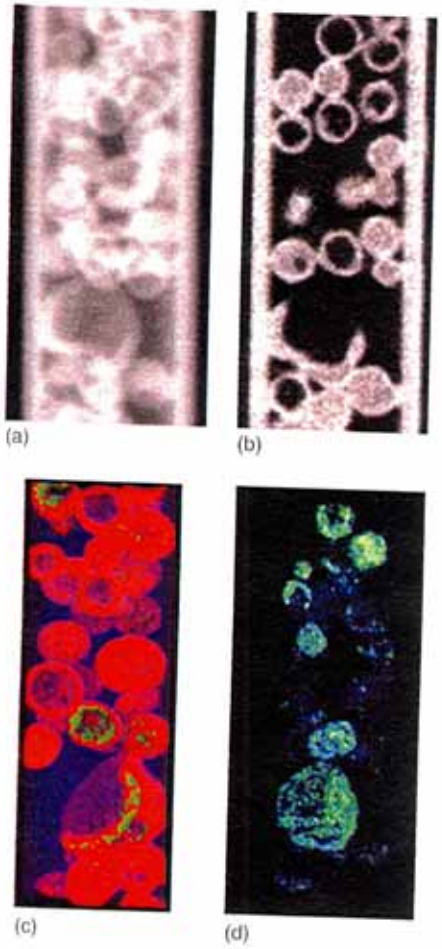

Figure 22.17 STXM tomography of polyacrylate-filled polystyrene microspheres in water in a pulled glass capillary [123]. (a) Projection image at 530.0 eV. (b) A 50 nm thick slice through the center of the tomographic reconstruction of 60 projections (0–180°/3°). (c) Colorized rendering of the reconstruction in which the PS (red) and water (blue) are differentiated by optical density at 530 eV, while the acrylate (green) is identified spectroscopically by the difference in OD at 532 and 530 eV. (d) Quantitative map of the acrylate component. The blue color scale corresponds to 2–8 nm of acrylate, and the green color scale corresponds to 8–15 nm in the projection. (From Ref. [123], used with permission from IUCr.)

relative ease with which the local sample environment can be adapted. The UHV requirements for SPEM and X-PEEM limit the flexibility to carry out experiments controlling the local chemical environment, and the strong fields at the sample in X-PEEM make it difficult to modify samples with applied electric or magnetic fields. In contrast, the photon-in/photon-out character of (S)TXM microscopes allow them to be readily adapted to make *in situ* modifications of the sample through controlled chemical, mechanical, thermal, or external fields. *In situ* experiments have been performed using electrochemistry [127], flow wet cells for chemical reaction [128], pulsed or AC current used for modifying magnetic properties [129], current flow in active semiconductor circuits [130], flow gas cells [131], variable humidity cells [90, 132], and variable temperatures [133].

Both TXM and STXM have been developed for magnetic dynamics experiments. While subnanosecond TXM experiments require few bunch operations to achieve subnanosecond time resolution, STXM techniques now exist to measure time-dependent magnetic properties of samples with 150 ps time resolution while the synchrotron is operating with full current in the multibunch mode. One very elegant recent example of this is the STXM study by Weigand *et al.* [129], which mapped the dynamics of switching of the out-of-plane magnetization (vortex core) caused by an applied AC current pulse (Figure 22.18). This experiment imaged and tracked with 250 ps time sampling and 10 nm positional precision the lateral position and polarity of the vortex core in a 500 nm permalloy pad after it was excited by different magnitudes of a GHz excitation pulse. The vortex core reversal was found to take place through coherent excitation by the leading and trailing edges of the pulse, which significantly lowered the field amplitude required for switching. The mechanism can be understood in terms of gyration around the vortex equilibrium positions, which are displaced by the applied field. The study showed that a much lower power is required to switch the polarity of the vortex

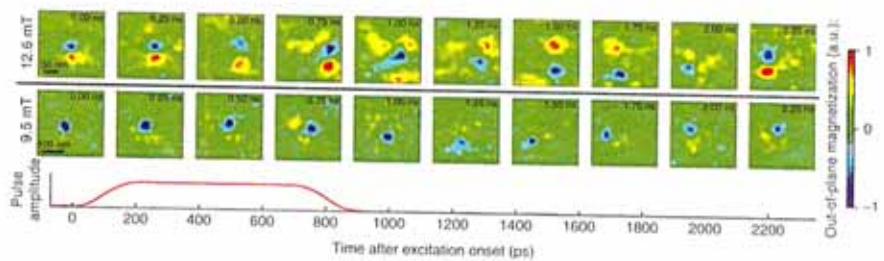

Figure 22.18 Use of time-resolved STXM to study the dynamics and mechanism of vortex core switching [129]. Each color-coded image shows successive 250 ps time steps of the out-of-plane magnetization of the center section of a 500 nm^2 permalloy element excited by in-plane magnetic pulses with a length of 700 ps. At 9.5 mT (below the switching threshold), the vortex core is displaced by the pulse and excited into gyrotropic gyration. At 12.6 mT (above the threshold), the dynamics of the two vortex core polarization states are superimposed, indicating vortex core switching. (From Ref. [129], *http://prl.aps.org/abstract/PRL/v102/i7/e077201*, copyright 2009 by the American Physical Society, used with permission.)

motion with an appropriately shaped pulsed field than with a DC field, thereby opening the possibility for practical magnetic storage or processing devices based on vortex polarity.

A second example of state-of-the-art *in situ* investigations is the work of the de Groot group, who have adapted STXM to study catalysts under realistic conditions of temperature and pressure [131, 134]. Figure 22.19a shows schematics of the catalyst cell that was built for both TEM and STXM use [135]. By using microfabrication techniques, heating is extremely localized and the whole structure is very compact and compatible with the spatial constrains of both STXM and TEM. While most of the Si_3N_4 support is thick, to be compatible with high pressure differentials (up to 2 bar), there are a series of 10 µm diameter holes between the heater traces where the Si_3N_4 has been further etched so as to be transparent to soft X-rays. There is provision for gas flow into the gap between the heater element and a cover window. Figure 22.19b,c presents localized Fe 2p NEXAFS spectra and color-coded component maps from a study of the evolution of an individual Fe-based Fischer–Tropsch synthesis catalyst particle during its activation phase (heating in atmospheric pressure of H_2 from ambient to 500 °C) [131]. Image sequences were recorded at the Fe 2p and O 1s edge as a function of temperature. Below 300 °C, the changes in the Fe catalyst were heterogeneous and depended on its interaction with the SiO_2 support. When the sample was heated further, the Fe environment became more homogeneous. By 450 °C, the catalyst consisted of Fe^0:Fe^{2+}:mixed Fe^{2+}/Fe^{3+} species in a ratio of about 1 : 1 : 1. Apparently, the enhanced mobility of Si species combined with the stabilization of Fe^{2+} leads to an almost homogeneous Fe distribution after reduction at this temperature. Fe^{2+} in close contact with SiO_2 is stabilized from further reduction to Fe^0.

22.5 Future Outlook and Summary

Soft X-ray microscopy has reached an intermediate phase of development where the major techniques – TXM, STXM, SPEM, and X-PEEM – are all well established with reliable and user-accessible instrumentation (see Table 22.1), which allows even inexperienced users to access its capabilities. The techniques have been applied to many different areas of science, medicine, and engineering, with a significant component of the work relying on materials characterization at the

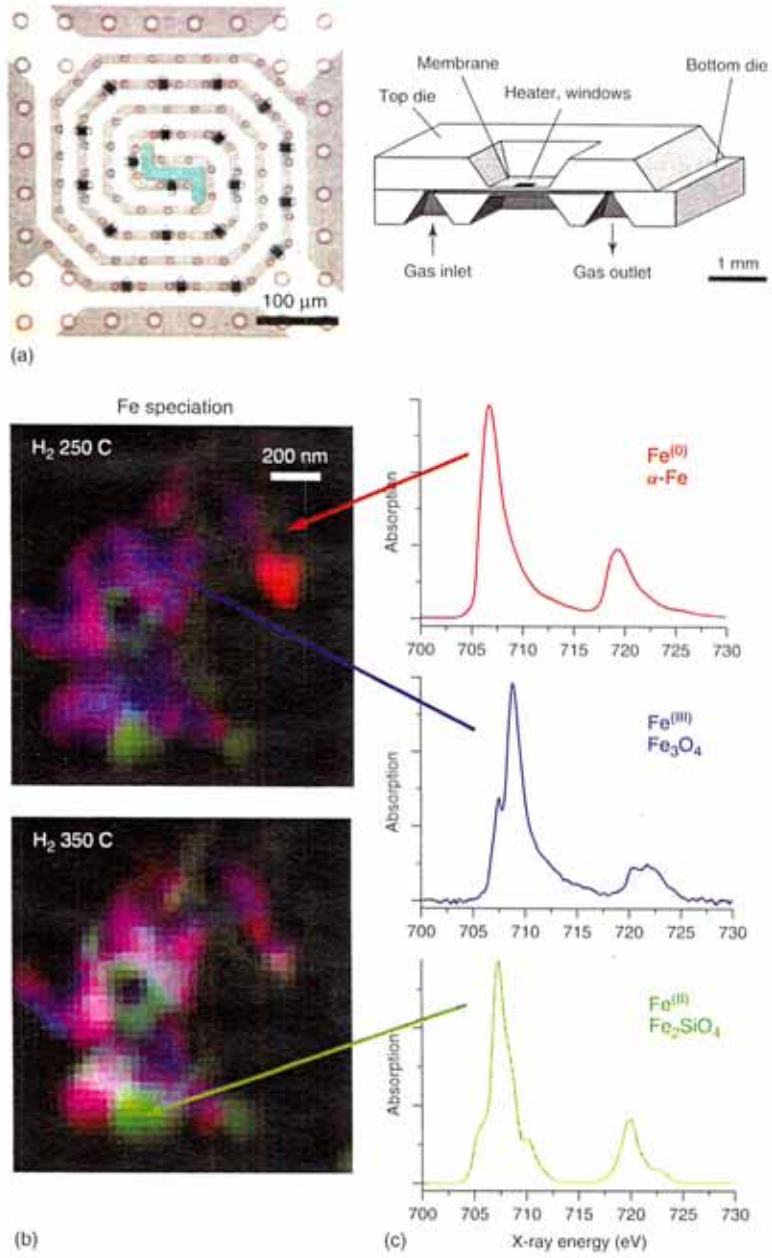

Figure 22.19 (a) *In situ* microheater on a Si_3N_4 support with 10 µm wide X-ray transparent windows, which is being used for STXM studies of catalyst and other materials at temperatures as high as 700 °C, with multiatmosphere pressures of gases [135]. (b) Evolution with temperature under an atmosphere of H_2 of the distribution of Fe chemical states in a single grain of a Fischer–Tropsch catalyst [131] – red = α – Fe, green = magnetite (Fe_3O_4), and blue = Fe_2SiO_4. (c) Fe 2p spectra from the indicated regions, which correspond to relatively pure domains of each species. (Part (a) from Ref. [131], permission granted from Ultramicroscopy via RightsLink license 2534321437193; parts (b,c) from F. de Groot, private communication, permission granted.)

sub-50 nm spatial scale. There is ongoing development of both the microscopes and the ancillary instrumentation and methodology that is needed to apply them to specific problems. In the area of instrumentation, there will be significant breakthroughs in X-PEEM in the next few years, with compensation of both spherical and chromatic aberrations achieving sub-10 nm spatial resolution. The TXM and STXM performance continuously improves with advances in ZP fabrication technology. At the Tenth International Conference of X-ray Microscopy (Chicago, August 2010), there were a number of presentations in which both KB mirror focusing and ZP optics achieved sub-10 nm performance with high-contrast test samples. Translating that capability to routine operation with lower contrast, real-world samples are needed. Challenging applications such as measurement of the magnetic properties of nanoscale materials – for example, measuring the XMCD signals of individual 30 nm magnetite magnetosomes in magnetotactic bacteria, which has recently been achieved for the first time, using STXM [136] – are useful to bridge from artificial test structures to real-world problems.

A large part of the scientific impact of nanoscopy with soft X-ray microscopies will be the result of innovation in the area of *in situ* control of the sample environment. There are many groups actively working in this area, so new and more powerful applications are to be expected. Finally, there is the issue of access. The community of soft X-ray microscopy users is fully saturating the existing synchrotron-based microscopes. These instruments are typically the ones most in demand at every synchrotron, as determined by the competitive peer review process that governs access. There is clearly a need for building and operating additional beamlines and more soft X-ray microscopes. The most successful of the current instruments are those which are on dedicated beamlines whose optical properties have been optimized for the type of microscopy involved. This trend continues. Given the relatively large number of recently completed third-generation synchrotrons (CLS, Soleil, Diamond, Australian Synchrotron, Alba, Shanghai, and PETRA) as well as those funded and under construction (NSLS II, Taiwan, Saga-LS, SuperSOR, PLS upgrade), most of which do or will have soft X-ray microscopic instrumentation, I am optimistic that access to soft X-ray microscopies will be significantly easier in the near future. Finally, with the recent successes of the fourth-generation light sources at Flash and LCLS, there will be a new frontier of soft X-ray imaging at the femtosecond time scale, most likely dominated by single-shot coherent diffraction techniques. X-ray microscopy is already a significant contributor to the field of nanoscopy and will become increasingly important in the future.

Acknowledgments

I thank my group members and collaborators and many others who have provided material for this review: Peter Fischer, Frank de Groot, Burkhard Kaulich, Maya Kiskanova, Carolyn Larabell, Hendrik Ohldag, Christoph Quitmann, Andreas Scholl, Jo Stöhr, Ben Watts, and Phil Withers. Research by my group was carried out at the ALS and CLS and was supported by NSERC (Canada) and the Canada Research Chair program. I especially thank Tolek Tyliszczak and David Kilcoyne for their contributions to developing and maintaining the STXM instruments at the ALS and Konstantin Kaznatcheev, Chithra Karunakaran, Jian Wang, Drew Bertwistle, and Yingshen Lu for developing and maintaining the CLS-SM beamline and STXM and PEEM instruments at the CLS. The ALS is supported by the Director, Office of Energy Research, Office of Basic Energy Sciences, Materials Sciences Division of the US Department of Energy, under Contract No. DE-AC03-76SF00098. The CLS is supported by NSERC, CIHR, NRC, and the University of Saskatchewan.

References

1. Bertsch, P.M. and Hunter, D.B. (2001) Applications of synchrotron-based x-ray microprobes. *Chem. Rev.*, **101**, 1809–1842.
2. Winick, H. (1995) *Synchrotron Radiation Sources: A Primer*, World Scientific, Singapore.
3. Attwood, D. (2000) *Soft X-rays and Extreme Ultraviolet Radiation, Principles and Applications*, Cambridge University Press.
4. Seres, J., Seres, E., Verhoef, A., Tempes, G., Streli, C., Wobrauschek, P., Yakovlev, V., Scrinzi, A., Spielmann, C., and Krausz, F. (2005) Source of coherent kiloelectronvolt X-rays. *Nature*, **433**, 596–598.
5. Bertilson, M., von Hofsten, O., Thieme, J., Lindblom, M., Holmberg, A., Takman, P., Vogt, U., and Hertz, H. (2009) First application experiments with the Stockholm compact soft x-ray microscope. Proceedings of the 9th International Conference on X-ray Microscopy, Zurich Switzerland, August 2008. *Journal of Physics: Conference Series*, **186**, 012025 - 1–012025-3.
6. Mainwaring, P. (2008) Application of the Gatan X-ray ultramicroscope to the investigation of material and biological samples. *Microsc. Today*, **16** (6) 14–17.
7. Kirz, J., Jacobsen, C., and Howells, M. (1995) Soft X-ray microscopes and their biological applications. *Q. Rev. Biophys.*, **28**, 33–130.
8. Ade, H. (1998) in *Experimental Methods in the Physical Sciences*, vol. **32** (eds J.A.R. Samson and D.L. Ederer), Academic Press, San Diego, CA, pp. 225–276.
9. Jacobsen, C. (1999) Soft X-ray microscopy. *Trends Cell Biol.*, **9**, 44–60.
10. Bauer, E. (2001) Photoelectron spectromicroscopy: present and future. *J. Electron. Spectrosc. Relat. Phenom.*, **114–116**, 975–987.
11. Bauer, E. (2001) Photoelectron microscopy. *J. Phys. Condens. Matter*, **13**, 11391–11404.
12. Guenther, S., Kaulich, B., Gregoratti, L., and Kiskinova, M. (2002) Photoelectron microscopy and applications in surface and material science. *Prog. Surf. Sci.*, **70**, 187–260.
13. Urquhart, S.G. and Ade, H. (2002) in *Chemical Applications of Synchrotron Radiation, Part I* (ed. T.K. Sham), World Scientific, Singapore, pp. 285–355.
14. Hitchcock, A.P., Stöver, H.D.H., Croll, L.M., and Childs, R.F. (2005) Chemical mapping of polymer microstructure using soft X-ray spectromicroscopy. *Aust. J. Chem.*, **58**, 423–432.
15. Howells, M., Jacobsen, C., and Warwick, T. (2007) in *Principles and Applications of Zone Plate X-Ray Microscopes in Science of Microscopy* (eds P. Hawkes and J. Spence), Springer, New York, pp. 835–926.
16. Ade, H. and Hitchcock, A.P. (2008) NEXAFS microscopy and resonant scattering: composition and orientation probed in real and reciprocal space. *Polymer*, **49**, 643–675.
17. Leung, B.O., Brash, J.L., and Hitchcock, A.P. (2010) Characterization of biomaterials by soft X-ray spectromicroscopy. *Materials*, **3**, 3911–3938.
18. Stöhr, J. and Siegmann, H.C. (2006) *Magnetism: From Fundamentals to*

Nanoscale Dynamics, Series in Solid - State Sciences, Springer, Berlin.

19. Huang, X., Nelson, J., Kirz, J., Lima, E., Marchesini, S., Miao, H., Neiman, A.M., Shapiro, D., Steinbrener, J., Stewart, A., Turner, J.J., and Jacobsen, C.J. (2009) Soft X-ray diffraction microscopy of a frozen hydrated yeast cell. *Phys. Rev. Lett.*, **103**, 198101 - 1–198101-4.
20. Bergh, M., Huldt, G., Timneanu, N., Filipe, R., Maia, N.C., and Hajdu, J. (2008) Feasibility of imaging living cells at subnanometer resolutions by ultrafast X-ray diffraction. *Q. Rev. Biophys.*, **41**, 181–204.
21. Withers, P.J. (2007) X-ray nanotomography. *Mater. Today*, **10**, 26–34.
22. Schmahl, G. and Rudolph, D. (1969) Lichstarke Zoneplatten als abbildende Sytee für weiche Röntgenstrahlung (High power zone plates a image forming systems for soft X-rays). *Optik*, **29**, 577–585.
23. Schmahl, G., Rudolph, D., Niemann, B., and Christ, O. (1980) Zone-plate X-ray microscopy. *Q. Rev. Biophys.*, **13**, 297–315.
24. Chao, W.L., Harteneck, B.D., Liddle, J.A., Anderson, E.H., and Attwood, D.T. (2005) Soft X-ray microscopy at a spatial resolution better than 15 nm. *Nature*, **435**, 1210–1213.
25. Chao, W., Kim, J., Rekawa, S., Fischer, P., and Anderson, E.H. (2009) Demonstration of 12 nm resolution fresnel zone plate lens based soft X-ray microscopy. *Opt. Express*, **17**, 17669–17677.
26. Rehbein, S., Heim, S., Guttmann, P., Werner, S., and Schneider, G. (2009) Ultrahigh-resolution soft-x-ray microscopy with zone plates in high orders of diffraction. *Phys. Rev. Lett.*, **103**, 110801 - 1–110801-4.
27. Fischer, P., Kim, D.H., Chao, W.L., Liddle, J.A., Anderson, E.H., and Attwood, D.T. (2006) Soft X-ray microscopy of nanomagnetism. *Mater. Today*, **9**, 26–33.
28. Meier, G., Bolte, M., Eiselt, R., Krüger, B., Kim, D.-H., and Fischer, P. (2007) Direct imaging of stochastic domain-wall motion driven by nanosecond current pulses. *Phys. Rev. Lett.*, **98**, 187202 - 1–187202-4.
29. Fischer, P., Kim, D.-H., Mesler, B.L., Chao, W.L., and Anderson, E.H. (2007) Magnetic soft X-ray microscopy: imaging spin dynamics at the nanoscale. *J. Magn. Magn. Mater.*, **310**, 2689–2692.
30. Kasai, S., Fischer, P., Im, M.-Y., Yamada, K., Nakatani, Y., Kobayashi1, K., Kohnoand, H., and Ono, T. (2008) Probing the spin polarization of current by soft X-ray imaging of current-induced magnetic vortex dynamics. *Phys. Rev. Lett.*, **101**, 237203 - 1–237203-4.
31. Gartner, E.M., Kurtis, K.E., and Monteiro, P.J.M. (2000) Proposed mechanism of C-S-H growth tested by soft X-ray microscopy. *Cement Concrete Res.*, **30**, 817–822.
32. Silva, D.A., and Monteiro, P.J.M. (2005) Analysis of C-S-H hydration using soft X-rays transmission microscopy: effect of EVA copolymer.. *Cement Concrete Res.*, **35**, 2026–2032.
33. Heim, S., Guttmann, P., Rehbein, S., Werner, S., and Schneider, G. (2009) Energy-tunable full-field x-ray microscopy: cryo-tomography and nano-spectroscopy with the new BESSY TXM. Proceedings of the 9th International Conference on X-ray Microscopy, Zurich Switzerland August 2008. *J. Phys.: Conf. Ser.*, **186**, 012041 - 1–012041-3.
34. Guttmann, P., Bittencourt, C., Ke, X., Van Tendeloo, G., Umek, P., Arcon, D., Ewels, C.P., Rehbein, S., Heim, S., and Schneider, G. (2011) TXM-NEXAFS of TiO2-based nanostructures. 10th International Conference on X-Ray Microscopy, Chicago, August 12–16, 2010, *Am. Inst. Phys. Conf. Proc.* **1365**, 437–440.
35. Kihara, H., Yamamoto, A., Guttmann, P., and Schmahl, G. (1996) Observation of the internal membrane system of COS cells by X-ray microscopy. *J. Electron. Spectrosc. Relat. Phenom.*, **80**, 369–372.

36. Born, M. and Wolf, E. (2003) *Principles of Optics: Electromagnetic Theory of Propagation, Diffraction and Interference of Light*, Cambridge University Press.
37. Guttmann, P., Zeng, X., Feser, M., Heim, S., Yun, W., and Schneider, G. (2009) Ellipsoidal capillary as condenser for the BESSY full-field x-ray microscope. Proceedings of the 9th International Conference X-Ray Microscopy, Zurich Switzerland, August 2008. *J. Phy.: Conf. Ser.*, **186**, 012064 - 1–012064-3.
38. Kaulich, B., Susini, J., David, C., Di Fabrizio, E., Morrison, G., Charalambous, P., Thieme, J., Wilhein, T., Kovac, J., Bacescu, D., Salome, M., Dhez, O., Weitkamp, T., Cabrini, S., Cojoc, D., Gianoncelli, A., Vogt, U., Podnar, M., Zangrando, M., Zacchigna, M., and Kiskinova, M. (2006) A European twin X-ray microscopy station commissioned at ELETTRA. Proceedings of the 8th International Conference on X-Ray Microscopy, IPAP Conference Proceedings Series 7 (eds S. Aoki, Kagoshima, Y. and Suzuki, Y.), pp. 22–25.
39. Wichtendahl, R., Fink, R., Kuhlenbeck, H., Preikszas, D., Rose, H., Spehr, R., Hartel, P., Engel, W., Schlögl, R., Freund, H.-J., Bradshaw, A.M., Lilienkamp, G., Schmidt, Th., Bauer, E., Brenner, G., and Umbach, E. (1998) SMART: an aberration-corrected XPEEMK/LEEM with energy filter. *Surf. Rev. Lett.*, **5**, 1249–1256.
40. Hartel, P., Preikszas, D., Spehr, R., Müller, H., and Rose, H. (2002) Mirror corrector for low-voltage electron microscopes. *Adv. Imaging Electron. Phys.*, **120**, 41–133.
41. Schmidt, Th., Marchetto, H., Lévesque, P.L., Groh, U., Maier, F., Preikszas, D., Hartel, P., Spehr, R., Lilienkamp, G., Engel, W., Fink, R., Bauer, E., Rose, H., Umbach, E., and Freund, H.-J. (2010) Double aberration correction in a low-energy electron microscope. *Ultramicroscopy*, **110**, 1358–1361.
42. Wan, W., Feng, J., Padmore, H.A., and Robin, D.S. (2004) Simulation of a mirror corrector for PEEM3. *Nucl. Instrum. Methods Phys. Res. A*, **519**, 222–229.
43. Feng, J., Forest, E., MacDowell, A.A., Marcus, M., Padmore, H., Raoux, S., Robin, D., Scholl, A., Schlueter, R., Schmid, P., Stöhr, J., Wan, W., Wei, D.H., and Wu, Y. (2005) An x-ray photoemission electron microscope using an electron mirror aberration corrector for the study of complex materials. *J. Phys C.: Condens. Matter*, **17**, S1339–S1350.
44. Feng, J. and Scholl, A. (2006) Photoemission electron microscopy (PEEM), in *Science of Microscopy* (eds P.W. Hawkes and J.C.H. Spence), Wiley-VCH Verlag GmbH, 657–695.
45. Haider, M., Uhlemann, S., Schwan, E., Rose, H., Kabius, B., and Urban, K. (1998) Electron microscopy image enhanced. *Nature*, **392**, 768–769.
46. Krivanek, O.L., Dellby, N., and Lupini, A.R. (1999) Towards sub-Å electron beams. *Ultramicroscopy*, **78**, 1–11.
47. Tromp, R., Hannon, J.B., Ellis, A.W., Wan, W., Berghaus, A., and Schaff, O. (2010) A new aberration-corrected, energy-filtered LEEM/PEEM instrument. I. Principles and design. *Ultramicroscopy*, **110**, 852–861.
48. Kilcoyne, A.L.D., Tylisczak, T., Steele, W.F., Fakra, S., Hitchcock, P., Franck, K., Anderson, E., Harteneck, B., Rightor, E.G., Mitchell, G.E., Hitchcock, A.P., Yang, L., Warwick, T., and Ade, H. (2003) Interferometer-controlled scanning transmission X-ray microscopes at the advanced light source. *J. Synchrotron Radiat.*, **10**, 125–136.
49. Warwick, T., Ade, H., Kilcoyne, A.L.D., Kritscher, M., Tylisczcak, T., Fakra, S., Hitchcock, A.P., Hitchcock, P., and Padmore, H.A. (2002) A new bend-magnet beamline for scanning transmission X-ray microscopy at the Advanced Light Source. *J. Synchrotron Radiat.*, **9**, 254–257.
50. Rarback, H., Shu, D., Feng, S.C., Ade, H., Kirz, J., McNulty, I., Kern, D.P., Chang, T.H.P., Vladimirsky, Y., Iskander, N., Attwood, D., McQuaid, K., and Rothman, S. (1988) Scanning X-ray microscope with 75-nm resolution. *Rev. Sci. Instrum.*, **59**, 52–59.

51. Thieme, J. (1988) Theoretical investigations of imaging properties of zone plates and zone plate systems using diffraction theory, in *Proceedings of the 2nd International Conference X-Ray Microscopy Stony Brook, USA, July 1987, X-ray Microscopy II* (eds D. Sayre, Howells, M. Kirz, J. and Rarback), H. Springer-Verlag, Berlin, 211–216.
52. Jacobsen, C., Wirick, S., Flynn, G., and Zimba, C. (2000) Soft X-ray spectroscopy from image sequences with sub-100 nm spatial resolution. *J. Microsc.*, **197**, 173–184.
53. Feser, M., Carlucci-Dayton, M., Jacobsen, C., Kirz, J., Neuhäusler, U., Smith, G., and Yu, B. (1998) Applications and instrumentation advances with the Stony Brook scanning transmission X-ray microscope. X-Ray Microfocusing: Applications and Techniques, San Diego California, July 22–23, 1998. *Proc. SPIE*, **3449**, 19–26.
54. Feser, M., Hornberger, B., Jacobsen, C., De Geronimo, G., Rehak, P., Holl, P., and Strüder, L. (2006) Integrating Silicon detector with segmentation for scanning transmission X-ray microscopy. *Nucl. Phys. Res. A*, **565**, 841–854.
55. Hornberger, B., Feser, M., and Jacobsen, C. (2007) Quantitative amplitude and phase contrast imaging in a scanning transmission X-ray microscope. *Ultramicroscopy*, **107**, 644–655.
56. Gianoncelli, A., Morrison, G.R., Kaulich, B., Bacescu, D., and Kovac, J. (2006) Scanning transmission x-ray microscopy with a configurable detector. *Appl. Phys. Lett.*, **89**, 251117 - 1–251117-3.
57. Maser, J., Osanna, A., Wang, Y., Jacobsen, C., Kirz, J., Spector, S., Winn, B., and Tennant, D. (2000) Soft X-ray Microscopy with a cryo scanning transmission X-ray microscope: I. Instrumentation, imaging and spectroscopy. *J. Microsc.*, **197**, 68–79.
58. Nolle, D., Weigand, M., Schütz, G., and Goering, E. (2011) High Contrast Magnetic and Nonmagnetic Sample Current Microscopy for Bulk and Transparent Samples Using Soft X-Rays. *Microsc. Microanal.*, **17**, 834–842.
59. Kilcoyne, A.L.D., Ade, H., Attwood, D. Hitchcock, A.P., McKean, P., Mitchell, G.E., Monteiro, P., Tyliszczak, T., and Warwick, T. (2010) A new Scanning Transmission X-ray Microscope at the ALS for operation up to 2500 eV. Proceedings of Synchrotron Radiation International, Melbourne, September 12–16, 2009. *AIP Conf. Proc.*, **1234**, 459–462.
60. Jacobsen, C., Lindaas, S., Williams, S., and Zhang, X. (1993) Scanning luminescence x-ray microscopy: imaging fluorescence dyes at suboptical resolution. *J. Microsc.*, **172**, 121–129.
61. Alberti, R., Longoni, A., Klatka, T., Guazzoni, C., Gianoncelli, A., Bacescu, D., and Kaulich, B. (2008) A low energy X-ray fluorescence spectrometer for elemental mapping X-scopy. IEEE Nuclear Science Symposium Conference, Record N14, pp. 31–33.
62. Alberti, R., Klatka, T., Longoni, A., Bacescu, D., Marcello, A., De Marco, A., Gianoncelli, A., and Kaulich, B. (2009) Development of a low-energy x-ray fluorescence system with sub-micrometer spatial resolution. *X-ray Spectrom.*, **38**, 205–210.
63. Gianoncelli, A., Kaulich, B., Alberti, R., Klatka, T., Longoni, A., De Marco, A., Marcello, A., and Kiskinova, M. (2009) Simultaneous soft X-ray transmission and emission microscopy. *Nucl. Instrum. Methods A*, **608**, 195–199.
64. Gianoncelli, A., Klatka, T. Alberti, R., Bacescu, D., De Marco, A., Marcello, A., Longoni, A., Kaulich, B., and Kiskinova, M. (2009) Development of a low-energy X-ray fluorescence system combined with X-ray microscopy. Proceedings of the 9th International Conference on X-ray Microscopy, Zurich Switzerland, August 2008. *J. Phys.: Conf. Ser.*, **186**, 012007 - 3.
65. Hitchcock, A.P., Tyliszczak, T., and Obst, M. (2012) Enhancing detection limits through X-ray fluorescence detection in soft X-ray scanning transmission X-ray microscopy. *Environmental Science and Technology*, in press.

66. Eguchi, T., Okuda, T., Matsushima, T., Kataoka, A., Harasawa, A., Akiyama, K., Kinoshita, T., Hasegawa, Y., Kawamori, M., Harujama, Y., and Matsui, S. (2006) Element specific imaging by scanning tunneling microscopy combined with synchrotron radiation light. *Appl. Phys. Lett.*, **89**, 2431191 - 1–2431191-3.
67. Ascensio, M.C., Imaging and nanoARPES: An innovative and powerful tool for the nanosciences, (2011) *Le Rayon de Soleil*, **21**, 4–6.
68. Schmid, I., Raabe, J., Fink, R.H., Wenzel, S., Hug, H., and Quitmann, C. (2011) Seeing and "feeling" polymer blends on a nano-scale. Proceedings of 10th International Conference on X-ray Microscopy, Chicago, August 14–18, 2010. *Am. Inst. Phys. Conf. Ser.*, **1365**, 449–452.
69. Susini, J., Somogyi, A., Barrett, R., Salomé, M., Bohic, S., Fayard, B., Eichert, D., Dhez, O., Bleuet, P., Martinez-Criado, G., and Tucoulou, R. (2004) The X-ray microscopy and micro-spectroscopy facility at the ESRF. Proceedings of International Symposium on Portable Synchrotron Light Sources and Advanced Applications, Shiga Japan, January 13–14. *AIP Conf. Proc.*, **716**, 18–21.
70. Kaulich, B., Gianoncelli, A., Beran A., Eichert, D., Kreft, I., Pongrac, P., Regvar, M., Vogel-Mikus, K., and Kiskinova, M. Low-energy (2009) X-ray fluorescence microscopy opening new opportunities for bio-related research. *J. R. Soc. Interface*, **6**, S641–S647.
71. Hitchcock, A.P., Tyliszczak, T., Obst, M., Swerhone, G.D.W., and Lawrence, J.R. (2010) Improving sensitivity in soft X-ray STXM using low energy X-ray fluorescence. *Microsc. Microanal.*, **16**, S - 2924–S-2925.
72. Kaulich, B., Bacescu, D., Cocco, D., Susini, J., David, C., DiFabrizio, E., Cabrini, S., Morrison, G., Thieme, J. Kiskinova, M. (2003) Twinmic: A European twin microscope station combining full-field imaging and scanning microscopy. Proceedings of 7th International Conference on X-Ray Microscopy ESRF, Grenoble, France, July 28 - August 2, 2002. *J Phys (France) IV*, **104**, 103–108.
73. Schmid, I., Raabe, J., Quitmann, C., Vranjkovic, S., Hug, H.J., Fink, R.H. (2009) NanoXAS, a novel concept for high resolution microscopy. Proceedings of the 9th Int. Conf. X-ray Microscopy, Aug 2008, Zurich, Switzerland. *J. Phys.: Conf. Ser.*, **186**, 012015 - 1–012015-3.
74. Schmid, I., Raabe, J., Sarafimov, B., Quitmann, C., Vranjkovic, S., Pellmont, Y., and Hug, H.J. (2010) Coaxial arrangement of a scanning probe and an X-ray microscope as a novel tool for nanoscience. *Ultramicroscopy*, **110**, 1267–1272.
75. Hanhan, S., Smith, A.M., Obst, M., and Hitchcock, A.P. (2009) Optimization of analysis of Ca 2p soft X-ray spectromicroscopy. *J. Electron. Spectrosc. Relat. Phenom.*, **173**, 44–49.
76. Sugiyama, M. and Sigesato, G. (2004) A review of focused ion beam technology and its applications in transmission electron microscopy. *J. Electron Microsc.*, **53**, 527–536.
77. De Stasio, G., Frazer, B.H., Gilbert, B., Richter, K.L., and Valley, J.W. (2003) Compensation of charging in X-PEEM: a successful test on mineral inclusions in 4.4 Ga old zircon. *Ultramicroscopy*, **98**, 57–62.
78. Zhang, X., Jacobsen, C., Lindaas, S., and Williams, S. (1995) Exposure strategies for PMMA from *in situ* XANES spectroscopy. *J. Vac. Sci. Technol. B*, **13**, 1477–1483.
79. Beetz, T. and Jacobsen, C. (2003) Soft X-ray radiation-damage studies in PMMA using a cryo-STXM. *J. Synchrotron Radiat.*, **10**, 280–283.
80. Wang, J., Morin, C., Hitchcock, A.P., Li, L., Zhang, X., Araki, T., Doran, A., and Scholl, A. (2009) Radiation damage in X-ray photoelectron emission microscopy: optimization for studies of radiation sensitive materials. *J. Electron. Spectrosc. Relat. Phenom.*, **170**, 25–36.
81. Leontowich, A.F.G. and Hitchcock, A.P. (2011) Zone plate focused soft X-ray lithography. *Appl. Phys. A: Mater. Sci. Process.*, **103** 1–11.

82. Wang, J., Botton, G.A., West, M.M., and Hitchcock, A.P. (2009) Quantitative evaluation of radiation damage to polyethylene terephthalate by soft X-rays and high energy electrons. *J. Phys. Chem. B*, **113**, 1869–1876.
83. Rightor, E.G., Hitchcock, A.P., Ade, H., Leapman, R.D., Urquhart, S.G., Smith, A.P., Mitchell, G.E., Fischer, D., Shin, H.J., and Warwick, T. (1997) Spectromicroscopy of poly(ethylene terephthalate): comparison of spectra and radiation damage rates in x-ray absorption and electron energy loss. *J. Phys. Chem. B*, **101**, 1950–1960.
84. Ade, H., Winesett, D.A., Smith, A.P., Qu, S., Ge, S., Sokolov, J., and Rafailovich, M. (1999) Phase segregation in polymer thin films: elucidations by X-ray and scanning force microscopy. *Europhys. Lett.*, **45**, 526–532.
85. Strang, G. (1988) *Linear Algebra and its Applications*, Harcourt Brace Jovanovich, San Diego, CA.
86. Press, W.H., Flannery, B.P., Teukolsky, S.A., and Vetterling, W.T. (1992) *Numerical Recipes in Fortran 77: The Art of Scientific Computing*, 2nd edn, Cambridge University Press.
87. Hitchcock, A.P. (2011) aXis2000 is free for noncommercial use. It is written in Interactive Data Language (IDL). *http://unicorn.mcmaster.ca/aXis2000.html* (accessed 15 December 2011).
88. Hitchcock, A.P., Dynes, J.J., Lawrence, J.R., Obst, M., Swerhone, G.D.W., Korber, D.R., and Leppard, G.G. (2009) Soft X-ray spectromicroscopy of nickel sorption in a natural river biofilm. *Geobiology*, **7**, 432–453.
89. Rousseau, M.E., Hernández Cruz, D., West, M.M., Hitchcock, A.P., and Pézolet, M. (2007) Nephilia clavipes spider dragline silk microstructure studied by scanning transmission X-ray microscopy. *J. Am. Chem. Soc.*, **129**, 3897–3905.
90. Lefevre, T., Pézolet, M., Hernández Cruz, D., West, M.M., Obst, M., Hitchcock, A.P., Karunakaran, C., and Kaznatcheev, K.V. (2009) Mapping molecular orientation in dry and wet dragline spider silk. Proceedings of the 9th International Conference X-ray Microscopy, August 2008, Zurich, Switzerland. *J. Phys.: Conf. Ser.*, **186**, 012089 - 1–012089-3.
91. Najafi, E., Hernández Cruz, D., Obst, M., Hitchcock, A.P., Douhard, B., Pireaux, J.-J., and Felten, A. (2008) Polarization dependence of the C 1s X-ray absorption spectra of individual multi-walled carbon nanotubes. *Small*, **4**, 2279–2285.
92. Felten, A., Gillon, X., Gulas, M., Pireaux, J.-J., Ke, X., Van Tendeloo, G., Bittencourt, C., Kilcoyne, A.L.D., Najafi, E., and Hitchcock, A.P. (2010) Measuring point defect density in individual carbon nanotubes using polarization-dependent X-ray microscopy. *ACS Nano*, **4**, 4431–4436.
93. Najafi, E., Wang, J., Hitchcock, A.P., Denommee, S., Ke, X., and Simard, B. (2010) Characterization of single-walled carbon nanotubes by scanning transmission X-ray spectromicroscopy: purification, order and dodecyl functionalization. *J. Am. Chem.*, **132**, 9020–9029.
94. Malinowski, E. (1991) *Factor Analysis in Chemistry*, 2nd ed, John Wiley & Sons, Inc., New York.
95. Lerotic, M., Jacobsen, C., Gillow, J.B., Francis, A.J., Wirick, S., Vogt, S., and Maser, J. (2005) Cluster analysis in soft X-ray spectromicroscopy: finding the patterns in complex specimens. *J. Electron. Spectrosc. Relat. Phenom.*, **144–147**, 1137–1143.
96. PCA_GUI and other useful IDL routines for analysis of soft X-ray microscopy data, *http://xrm.phys.northwestern.edu* (accessed 24 February 2011).
97. Koprinarov, I.N., Hitchcock, A.P., Li, W.H., Heng, Y.M., and Stöver, H.D.H. (2001) Quantitative compositional mapping of core-shell polymer microspheres by soft X-ray spectromicroscopy. *Macromolecules*, **34**, 4424–4429.
98. Urquhart, S.G. and Ade, H. (2002) Trends in the carbonyl core (C1s, O1s) $\rightarrow \pi^*_{C=O}$ transition in the near edge X-ray absorption fine structure spectra of organic molecules. *J. Phys. Chem. B*, **106**, 8531–8538.
99. Urquhart, S.G., Hitchcock, A.P., Smith, A.P., Ade, H.W., Lidy, W., Rightor, E.G., and Mitchell, G.E. (1999) NEXAFS spectromicroscopy of polymers: overview and quantitative analysis of polyurethane polymers. *J. Electron. Spectrosc. Relat. Phenom.*, **100**, 119–135.
100. Hitchcock, A.P., Koprinarov, I., Tyliszczak, T., Rightor, E.G., Mitchell, G.E., Dineen, M.T., Heyes, F., Lidy, W., Priester, R.D., Urquhart, S.G., Smith, A.P., and Ade, H. (2001) Optimization of scanning transmission x-ray microscopy for the identification and quantitation of reinforcing particles in polyurethanes. *Ultramicroscopy*, **88**, 33–49.
101. Mitchell, G.E., Wilson, L.R., Dineen, M.T., Urquhart, S.G., Hayes, F., Rightor, E.G., Hitchcock, A.P., and Ade, H. (2002) Quantitative characterization of microscopic variations in the cross-link density of gels. *Macromolecules*, **35**, 1336–1341.
102. Rightor, E.G., Urquhart, S.G., Hitchcock, A.P., Ade, H., Smith, A.P., Mitchell, G.E., Priester, R.D., Aneja, A., Appel, G., Wilkes, G., and Lidy, W.E. (2002) Identification and quantitation of urea precipitates in flexible polyurethane foam formulations by X-ray spectromicroscopy. *Macromolecules*, **35**, 5873–5882.
103. Croll, L.M., Stöver, H.D.H., and Hitchcock, A.P. (2005) Composite tectocapsules containing porous polymer microspheres as release gates. *Macromolecules*, **38**, 2903–2910.
104. Martin, Z., Jimenez, I., Gomez, M.A., Ade, H., and Kilcoyne, D.A. (2010) Interfacial interactions in PP/MMT/SEBS nanocomposites. *Macromolecules*, **43**, 448–453.
105. Martin, Z., Jiménez, I., Gómez-Fatou, M.A., West, M., and Hitchcock, A.P. (2011) Interfacial Interactions in Polypropylene-Organoclay-Elastomer nanocomposites: influence of polar modifications on the location of the clay. *Macromolecules*, **44**, 2179–2189.
106. Hoppe, H. and Sariciftci, N.S. (2004) Organic solar cells: an overview. *J. Mater. Res.*, **19**, 1924–1945.
107. McNeill, C.R., Watts, B., Thomsen, L., Belcher, W.J., Greenham, N.C., and Dastoor, P.C. (2006) Nanoscale quantitative chemical mapping of conjugated polymer blends. *Nano Lett.*, **6**, 1202–1206.
108. McNeill, C.R., Watts, B., Thomsen, L., Belcher, W.J., Kilcoyne, A.L.D., Greenham, N.C., and Dastoor, P.C. (2006) X-ray spectromicroscopy of polymer/fullerene composites: quantitative chemical mapping. *Small*, **2**, 1432–1435.
109. Watts, B., Schuettfort, T., and McNeill, C.R. (2011) Mapping of domain orientation and molecular order in polycrystalline semiconducting polymer films with soft x-ray microscopy. *Adv. Funct. Mater.* **21** 1122–1131.
110. Thibault, P., Dierolf, M., Menzel, A., Bunk, O., David, C., and Pfeiffer, F. (2008) High-resolution scanning X-ray diffraction microscopy. *Science*, **321**, 379–382.
111. Araki, T., Ade, H., Stubbs, J.M., Sundberg, D.C., Mitchell, G.E., Kortright, J.B., and Kilcoyne, A.L.D. (2006) Soft X-ray resonant scattering of structured polymer nanoparticle. *Appl. Phys. Lett.*, **89**, 1241061 - 1–1241061-3.
112. Mitchell, G.E., Landes, B.G., Lyons, J., Kern, B.J., Devon, M.J., Koprinarov, I., Gullikson, E.M., and Kortright, J.B. (2006) Molecular bond selective x-ray scattering for nanoscale analysis of soft matter. *Appl. Phys. Lett.*, **89**, 0441011 - 1–0441011-3.
113. Ohldag, H., van der Laan, G., and Arenholz, E. (2009) Correlation of crystallographic and magnetic domains at Co/NiO(001) interfaces. *Phys. Rev. B*, **79**, 052403 - 1–052403-4.
114. Leung, B.O., Wang, J., Brash, J.L., Hitchcock, A.P., Cornelius, R., Doran, A., and Scholl, A. (2009) An X-ray spectromicroscopy study of protein adsorption to a polystyrene-polylactide blend. *Biomacromolecules*, **10**, 1838–1845.
115. Gleber, S.-C., Sedlmair, J., Bertilson, M., von Hofsten, O., Heim, S., Guttmann, P., Hertz, H.M., Fischer, P.,

and Thieme, J. (2009) X-ray stereo microscopy for investigation of dynamics in soils. Proceedings of the 9th International Conference on X-ray Microscopy, Zurich Switzerland, August 2008. *J. Phys.: Conf. Ser.*, **186**, 012104 - 3.

116. Hitchcock, A.P., Araki, T., Ikeura-Sekiguchi, H., Iwata, N., and Tani, K. (2003) 3d chemical mapping of toners by serial section scanning transmission X-ray microscopy. Proceedings of the 7th International Conference on X-ray Microscopy, Grenoble France August. *J. Phys. IV France*, **104**, 509–512.
117. Le Gros, M.A., McDermott, G., and Larabell, C.A. (2005) X-ray tomography of whole cells. *Curr. Opin. Struct. Biol.*, **15**, 593–600.
118. Uchida, M., Sun, Y., McDermott, G., Knoechel, C., Le Gros, M.A., Parkinson, D., Drubin, D.G., and Larabell, C.A. (2011) Quantitative analysis of yeast internal architecture using soft X-ray tomography. *Yeast*, **28** 227–236.
119. Schneider, G., Guttmann, P., Heim, S., Rehbein, S., Mueller, F., Nagashima, K., Heymann, J.B., Müller, W.G., and McNally, J.G. (2010) Three-dimensional cellular ultrastructure resolved by X-ray microscopy. *Nat. Methods*, **7**, 985–987.
120. Carrascosa, J.L., Javier Chichón, F., Pereiro, E., Rodríguez, M.J., Fernández, J.J., Esteban, M., Heim, S., Guttmann, P., and Schneider, G. (2009) Cryo-x-ray tomography of Vaccinia Virus membranes and inner compartments. *J. Struct. Biol.*, **168**, 234–239.
121. Haddad, W.S., Trebes, J.E., Goodman, D.M., Lee, H.-R., McNulty, I., Anderson, E.H., and Zalensky, A.O. (1995) Ultrahigh-resolution soft x-ray tomography. X-ray Microbeam Technology and Applications, San Diego, CA. *Proc. SPIE*, **2516**, 102–107.
122. Wang, Y., Jacobsen, C., Maser, J., and Osanna, A. (2000) Soft x-ray microscopy with a cryo STXM: II. Tomography. *J. Microsc.*, **197**, 80–93.
123. Johansson, G.A., Tyliszczak, T., Mitchell, G.E., Keefe, M., and Hitchcock, A.P. (2007) Three dimensional chemical mapping by scanning transmission X-ray spectromicroscopy. *J. Synchrotron Radiat.*, **14**, 395–402.
124. Obst, M., Wang, J., and Hitchcock, A.P. (2009) 3-d chemical imaging with STXM tomography. Proceedings of the 9th International Conference X-ray Microscopy, August 2008, Zurich, Switzerland. *J. Phys.: Conf. Ser.*, **186**, 012045 - 1–012045-3.
125. Obst, M., Wang, J., and Hitchcock, A.P. (2009) Soft X-ray spectro-tomography study of cyanobacterial biomineral nucleation. *Geobiology*, **7**, 577–591.
126. Wang, J., Hitchcock, A.P., Karunakaran, C., Prange, A., Franz, B., Harkness, T., Lu, Y., Obst, M., and Hormes, J. (2011) 3D chemical and elemental imaging by STXM spectro-tomography. Proceedings of 10th International Conference on X-ray Microscopy. *Am. Inst. Phys. Conf. Ser.*, **1365** 215–218.
127. Guay, D., Stewart-Ornstein, J., Zhang, X., and Hitchcock, A.P. (2005) In situ spatial and time resolved studies of electrochemical reactions by scanning transmission X-ray microscopy. *Anal. Chem.*, **77**, 3479–3487.
128. Neuhäusler, U., Jacobsen, C., Schulze, D., Stott, D., and Abend, S. (2000) A specimen chamber for soft x-ray spectromicroscopy on aqueous and liquid samples. *J. Synchrotron Radiat.*, **7**, 110–112.
129. Weigand, M., Van Waeyenberge, B., Vansteenkiste, A., Curcic, M., Sackmann, V., Stoll, H., Tyliszczak, T., Kaznatcheev, K., Bertwistle, D., Woltersdorf, G., Back, C.H., and Schütz, G. (2009) Vortex core switching by coherent excitation with single in-plane magnetic field pulses. *Phys. Rev. Lett.*, **102**, 077201 - 1–077201-4.
130. Schneider, G., Rudolph, S., Meyer, A.M., Zschech, E., and Guttmann, P. (2005) X-ray microscopy: a powerful tool for electromigration studies in modern ICs. *Future Fab Int.*, **19**, 115–117.
131. de Smit, E., Swart, I., Creemer, J.F., Karunakaran, C., Bertwistle, D., Zandbergen, H.W., de Groot, F.M.F., and Weckhuysen, B.M. (2009)

Nanoscale chemical imaging of the reduction behavior of a single catalyst particle. *Angew. Chem. Int. Ed.*, **48**, 3632–3636.
132. Zhou, J., Wang, J., Fang, H., and Sham, T.-K. (2011) Investigating structural variation and water adsorption of SnO_2 coated carbon nanotube by nanoscale chemical imaging. *J. Mat. Chem.*, **21** 14622–14630.
133. Drake, I.J., Liu, T.C.N., Gilles, M.K., Tyliszczak, T., Kilcoyne, A.L.D., Shuh, D.K., Mathies, R.A., and Bell, A.T. (2004) An In-situ cell for characterization of solids by soft X-ray absorption. *Rev. Sci. Inst.*, **75**, 3242–3247.
134. de Smit, E., Swart, I., Creemer, J.F., Hoveling, G.H., Gilles, M.K., Tyliszczak, T., Kooyman, P.J., Zandbergen, H.W., Morin, C., Weckhuysen, B.M., and de Groot, F.M.F. (2008) Nanoscale chemical imaging of a working catalyst by scanning transmission X-ray microscopy. *Nature*, **456**, 222–225.
135. Creemer, J.F., Helveg, S., Hoveling, G.H., Ullmann, S., Molenbroek, A.M., Sarro, P.M., and Zandbergen, H.W. (2008) Atomic-scale electronmicroscopy at ambient pressure. *Ultramicroscopy*, **108**, 993–998.
136. Lam, K.P., Hitchcock, A.P., Obst, M., Lawrence, J.R., Swerhone, G.D.W., Leppard, G.G., Tyliszczak, T., Karunakaran, C., Wang, J., Kaznatcheev, K., Bazylinski, D., and Lins, U. (2010) X-ray magnetic circular dichroism of individual magnetosomes by Scanning Transmission X-ray Microscopy. *Chem. Geol.*, **270**, 110–116.